© 2022. This manuscript version is made available under the CC-BY-NC-ND 4.0 license https://creativecommons.org/licenses/by-nc-nd/4.0/. This is the accepted manuscript version of this paper, the final version (version of record) is available at https://doi.org/10.1016/j.rse.2022.113255

Sentinel-2 high-resolution data for river discharge monitoring

Paolo Filippucci (1, 3, 4), Luca Brocca (1), Stefania Bonafoni (2), Carla Saltalippi (3), Wolfgang Wagner (4), Angelica Tarpanelli (1)

1. National Research Council, Research Institute for Geo-Hydrological Protection, Perugia, Italy (paolo.filippucci@irpi.cnr.it)
2. Università degli Studi di Perugia, Department of Engineering, Perugia, Italy
3. Università degli Studi di Perugia, Department of Civil and Environmental Engineering, Perugia, Italy
4. TUWien (Technische Universität Wien), Department of Geodesy and Geoinformation, Wien, Austria

Abstract

River monitoring is an open issue due to many intrinsic problems of the ground monitoring network. Over the last few decades, the role of satellite sensors in river discharge estimation is significantly increased thanks to the strong growth in technologies and applications. Focusing on daily river discharge measurements, a non-linear regression model has been used to link the near-infrared (NIR) reflectance ratio between a dry and a wet pixel around the section of a river to the ground measurements of river discharge. The use of medium-resolution satellite data, such as those from MODIS sensors, enables to monitor high and low flows in medium-sized catchments (<100’000 km^2), thanks to satellite frequent revisit time and wide spatial coverage. However, such sensors are not suitable to provide information for medium-narrow rivers (< 250 m wide), nor to study river features and patterns that are averaged within a single pixel. Here, we investigated the use of Sentinel-2 NIR reflectances to support the hypothesis that a higher spatial resolution, i.e. 10 m, is able to better identify the wet pixels, more related to the river dynamics, with obvious advantages for river discharge estimation compared to the medium resolution sensors (e.g., MODIS at 250 m). Moreover, it also allows both a finer distinction between vegetation, soil and water and the characterization of water turbidity in the river area. A new formulation enriched by the sediment component is proposed together with a first step towards an uncalibrated procedure to select the wet pixels. Google Earth Engine (GEE) platform has been employed for the data analysis, allowing to avoid the download of big amounts of data, fostering the reproducibility of the analysis in different locations. The accuracy of the river discharges derived from Sentinel-2 reflectances is evaluated against the in-situ observations from selected gauging stations along two Italian rivers, Po and Tiber. The results confirm the good performances obtained with high-resolution images over the Po River, with average Nash-Sutcliffe efficiency ranging between 0.39 and 0.56 for the different configurations adopted. Relatively worse results were obtained over the Tiber River where the Nash-Sutcliffe efficiency ranged between 0.2 and 0.61, due to an issue on the registration of Sentinel-2 images.

Keywords: NIR reflectance, river discharge, Sentinel-2, sediment transport, Google Earth Engine, MODIS

1. Introduction

River discharge is one of the Essential Climate Variables, which contribute most to the characterization of Earth’s climate and its changes, as recognized by the Global Climate Observing Systems. On long time scales, the knowledge of river discharge values is important to identify potential effects of climate change over lands and ocean, since their changes could affect both ocean salinity and thermohaline circulation (Nohara et al. 2006; Piecuch et al., 2018; Ahmed et al., 2020). In shorter terms, it is a variable fundamental for the water cycle closure and for numerous applications of water management and related services, including flood protection (Hannah et al., 2011).

Currently, in-situ measurements are the most cost-effective and reliable option for river discharge monitoring (Fekete et al., 2015). However, there are still many rivers where discharge estimates either do not exist or are not promptly available, sometimes due to economic or political reasons (Fekete and Vörösmarty, 2007). This is particularly true in developing countries, even if the number of working gauging stations is declining worldwide (Crochemore et al., 2020; Vörösmarty et al., 2001).

Earth Observation (EO) data are currently a valuable source of information capable to support ground-based networks. In recent years, several approaches have been developed to infer river discharge information from satellite data. These techniques can be divided into those that need to be calibrated against observed data and those that do not require calibration and can therefore be applied even in ungauged basins (Gleason and Durand, 2020). The latter approaches use as input only remote sensing data or other global data that are independent of specific calibration. River discharge can thus be obtained using different paradigms. Some studies focus on developing hydrologic models to parse the components of the hydrologic cycle (precipitation, evapotranspiration, terrestrial storage) obtained by remote sensing and derive river discharge from the associated water excess (e.g. Emery et al., 2018; Lopez et al., 2017; Parr et al., 2015). An other paradigm consists of exploiting the laws of fluid mechanic to develop hydraulic models that can infer river discharge from hydraulic variables, such as elevation, slope, and width (e.g. Larnier et al., 2020; Oubanas et al., 2018). Finally, Mass conserved Flow law Inversions (McFlI, Gleason et al., 2017) applied to flow equations like the Manning's equation (e.g. Durand et al., 2014; Garambois and Monnier, 2015) or hydraulic geometric power laws (e.g. Feng et al., 2019; Gleason and Smith, 2014) can be exploited to infer river discharge in ungauged rivers. In all of these cases, the obtained river discharge is typically characterized by low accuracy, because the problem of uncalibrated river discharge estimation is basically ill posed: critical variables for accurately measuring river discharge, such as bathymetry or friction, cannot be measured by remote sensing (Gleason and Durand, 2020). Nonetheless, uncalibrated models can improve the scarce information available on ungauged rivers, thus even inaccurate models are useful. Alternatively, in-situ surveys and Unmanned Aerial Vehicles (UAVs) can be exploited to obtain additional information on ungauged river systems (Yang et al., 2019), also coupled with satellite data (Lou et al., 2020; Wufu et al., 2021), thus improving the obtained performance.

Calibrated approaches are usually more reliable, being adjusted using in-situ data or calibrated hydrologic models. They are mainly useful for extending the knowledge of river discharge in space and time. The majority of EO satellite-based techniques to retrieve river discharge belong to this category, according to different paradigms. Calibrated hydrologic models can be used to improve the knowledge of river discharge as, e.g., in Dziubanski et al. (2016), where a hydrologic model with a remote sensing-based snow routine is used to improve river discharge estimation for seven watersheds in the Upper Mississippi River basin. This is just one example of a rich literature where one or more satellite products are used in calibration/assimilation to retrieve river discharge information not only at regional (Jodar et al., 2018; Syed et al., 2005; Wulf et al., 2016) but also at global scale (Chandanpurker et al., 2017; Lin et al., 2019; Zhang et al., 2016). Hydraulic models are also widely used (e.g., Bjerklie et al., 2003; 2005; De Frasson et al., 2019), sometimes coupled with hydrological modeling (e.g., Neal et al., 2009). Finally, many calibrated methodologies for estimating river discharge are based on the concept of the space-based rating curves. In these approaches, satellite measurements of river level, river width or other empirical fluvial geomorphic phenomena are coupled with observed river discharge data to calibrate empirical relationships that can be used to effectively estimate river discharge from remote sensing data. In this framework, radar altimetry and optical sensor measurements are the most promising source of data, although microwave data are sometimes used as well (Brakenridge et al., 2007; Huo et al., 2021). Altimetric data are widely used because of the direct relation between stage and river discharge (Abdalla et al., 2021; Belloni et al., 2021; Paris et al., 2016; Tourian et al., 2013; Zakharova et al., 2020), but the spatial-temporal sampling of the altimetry missions is currently a limitation, leading to the need of applying different strategies to densify the data (Tourian et al., 2016; 2017**;** Boergens et al., 2017; Schwatke et al., 2015). As already demonstrated, if the altimetry is combined with other satellite information, the estimation of river flow is improved (see Tarpanelli et al., 2021 for a review). In this respect, satellite optical sensors play an important role together with radar altimetry for improving the river monitoring. Specifically, water and soil are rather distinguishable from optical data (Yang et al., 2020). River width measurements can therefore be extracted from cloud-free images by exploiting these differences. River discharge measurements can be then obtained from the river width by using empiric formulas, rating curves or models (Elmi et al., 2021; Pavelsky et al., 2014), also in combination with altimetric data (Sichangi et al., 2016). Notwithstanding this, the measurement is possible only in free clouds days (reducing the temporal availability of the obtained datum) and there are often misclassifications of water pixels due to cloud shadows or in areas characterized by steep terrain or dense urban environments (Mueller et al., 2016).

Focusing on daily measurements of river discharge, Tarpanelli et al. (2013; 2017; 2020) used passive MODIS remote sensing data to develop a linear regression approach first introduced by Brakenridge et al. (2007), which is effectively able to monitor high and low flow in medium basins (<100’000 km^2). The approach (hereafter named CM) is based on the different behavior in the NIR region between a Calibration (C) and a Measurement (M) pixels chosen over land and water, respectively. Indeed, in a bare soil or urban area, the C pixel has a reflectance behavior stable in time, while a pixel around the bank of a river, often inundated, has generally lower reflectance values that are inversely proportional to river discharge (Tarpanelli et al., 2013; 2017). Both pixels are affected by noises due to different sources, such as the atmosphere or the acquiring process, but the calculation of their ratio allows to account for them and therefore it is well correlated with the in-situ measurements of river discharge. Notwithstanding this, the presence of sediments in the river induces an increase in the water reflectance, which corresponds to an underestimation of the river discharge assessed through CM approach. The analysis of this phenomenon for medium-narrow rivers (100 - 300 m) can be facilitated by the use of high-resolution multispectral sensors to better represent the dynamic of such rivers. With respect to the medium resolution images used so far (i.e., MODIS, MERIS and OLCI), data with higher spatial resolution coming from the new launched Sentinel-2 Mission of the Copernicus European Earth Observation programme (10, 20 and 60 m spatial resolution), have opened new possibilities to investigate small targets. The CM approach has been already tested with the Sentinel-2 high-resolution data harmonized with Landsat-8 images in the Murray-Darling basin in Australia, with encouraging results (Shi et al., 2020) but for a short period of time (only one water year was considered) and by considering only a single pixel M of 30x30 m. Moreover, Shi et al. indicated as a potential issue the high presence of sediment in the river water during floods events, which introduce a source of noise in the M signal and consequently in the obtained river discharge.

Based on these premises, the first objective of this paper was to understand the benefits of high-resolution imagery by Sentinel-2 by extending the procedure to small targets and testing its limitations. For this purpose, two Italian rivers were selected as study areas: the Po River in northern Italy and the Tiber River in central Italy. The first one was selected due to its medium-narrow size and the availability of multiple stations with a dense record of hydraulic variables, while the second one was selected for its width of about 50-80 m. In particular, a total of seven stations were selected: five stations along the Po River (Piacenza, Cremona, Borgoforte, Sermide and Pontelagoscuro) and two stations along the Tiber River (Montemolino and Ponte Felice). In order to check the effective advances of the Sentinel-2 spatial resolution with respect to medium resolution, the same analyses were carried out also using MODIS product as input. As second objective, we attempted to improve the estimation of river discharge by implementing modifications at the original CM approach related to the impact of the solid transport. Finally, we moved a first step towards an uncalibrated procedure by selecting the sensitive pixels to the river discharge variations through an analysis of their correlations against land and water pixels.

In order to foster the analysis to large time scales and in several areas, the code was implemented in the Google Earth Engine, GEE, platform (Gorelick et al., 2017), reducing by far the computational time and storage capacities required to download images and apply the methodology.

The paper is structured as follows: the study areas with the satellite and ground datasets are introduced in Section 2, together with the cloud platform GEE. In Section 3, the CM approach and the proposed modifications are described. A sensitivity analysis of the threshold adopted within the approaches is carried out in Section 4, together with the results of the proposed models application on the sections of the two rivers. Finally, in Section 5 the conclusions of the analysis are summarized, including limitations and future developments of the procedure.

2. Study area & Data

2.1 Study area

The analysis is focused on seven sites located in Italy: five along the Po River at the stations of Piacenza (45.11 °N, 9.64 °E), Cremona (45.13 °N, 9.97 °E), Borgoforte (45.04 °N, 10.81 °E), Sermide (44.99 °N, 11.33

°E) and Pontelagoscuro (44.89 °N, 11.60 °E) and the two along the Tiber River at the stations of Montemolino (42.80 °N, 12.40 °E) and Ponte Felice (41.95 °N, 12.50°E). These sites were selected on the basis of the availability of in-situ flow measurements during the analyzed periods (2015-2020), the different regime of flow and the width of the river, which is medium-small.

The Po River is located in Northern Italy and it has a drainage area of 74'000 km^2: it is the longest Italian river and the fifth European river for river discharge. During the analyzed period the average discharge value at the five stations varies between 818 and 1312 m^3/s, with the minimum and the maximum values being equal to 242 and 8950 m^3/s, respectively. The maximum cross-section width at the bankfull discharge is around 500 m (Domeneghetti et al., 2018), during the seasonal peaks in spring (May-June) and autumns (November). The river discharge data are available online from the website of the Regional Agency for Environmental Protection (www.arpae.it/documenti.asp).

The Tiber River in central Italy has a drainage area of 17'375 km^2 and its average river discharge is much smaller than the one of the Po River: during the analyzed period, it is around 30.4 m^3/s at Montemolino and 117.2 m^3/s at Ponte Felice, with the minimum and maximum extremes being equal to 1.6 and 804.2 m^3/s, respectively, for Montemolino station and equal to 49.4 and 843.3 m^3/s, respectively, for Ponte Felice station. The river width varies between about 50 and 80 meters, surrounded by riparian vegetation. The data of Montemolino are provided by the Department of Environment, Planning and Infrastructure of the Umbria Region, which is in charge for the collection of hydro meteorological data in the Umbria Region, while those of Ponte Felice are made available from the Department of Environment, Planning and Infrastructure of the Lazio Region.

2.2 Satellite Near Infrared data

In order to assess the benefits deriving from the use of high spatial resolution imagery in estimating river discharge, two datasets of NIR data characterized by high and medium spatial resolution were selected from Sentinel-2 and MODIS sensors, respectively.

The Sentinel-2 mission is composed of two satellites, Sentinel-2A (launched on the 23 June 2015) and Sentinel-2B (launched on 7 March 2017). The satellites are placed in the same sun-synchronous orbit, phased 180° to each other. This strategy permits to increase the revisit time of Sentinel-2 from 10 days (using one satellite) to 5 days (using both of them), with increased revisit frequency in the areas where adjacent orbits overlap. Each satellite carries a MultiSpectral Instrument (MSI) sensor, capable of sensing electromagnetic radiations in 13 spectral bands, from visible to short-wave infrared. In this analysis, data from band 8 (central wavelength ~833 nm, bandwidth=106 nm) are selected, characterized by a spatial resolution of 10 meters. Two products are available: Level-1C product with orthorectified TOA (Top-Of-Atmosphere) reflectance and Level-2A product with surface reflectance. Generally, the atmospheric correction applied to produce the Level-2 product over land is different from the one applied over ocean/sea. The river is a fairly complex and mixed environment to be managed. In the absence of detailed studies on this, and because the effects of the atmosphere in clear-sky conditions can be assumed negligible when computing the ratio of neighboring pixels in the same area (as used in this study, see Section 3), we performed the analysis by using Level-1C product.

MODIS is a multispectral sensor on-board the TERRA and AQUA satellites, launched on the 18 December 1999 and the 4 May 2002, respectively, and capable of acquiring Earth's surface data at 36 different spectral bands with spatial resolution ranging from 250 to 1000 m at daily time scale. In the present study, the reflectance in band 2 (Near-Infrared, central wavelength ~859 nm, bandwidth=35 nm) of level-2 product MYD09GQ version 6 at 250 m of spatial resolution were considered. For cloud masking, the "state_1km" band of MYD09GA version 6 product was selected. Both the products come from the MODIS sensor onboard AQUA satellite.

The dimension of each Sentinel-2 image (~600 MB) and the number of images to be downloaded for a temporal analysis, make the process of collecting and reading the data not easy and computationally challenging. In order to show the method and illustrate the new algorithm, we referred to the Sentinel-2 data Level-1C for bands 8 dataset, provided by the Meteorological Environmental Earth Observation (MEEO – www.meeo.it) company, together with the relative cloud mask probability product. This collection includes a subset of Pontelagoscuro area in the period January 2018 – September 2019 and it is used to generate the figures shown in the Section 3. However, Google Earth Engine platform was used for the analysis relative to the period 2015-2020 over the seven stations for both the MODIS and Sentinel-2 analysis, in order to lighten the computational load: the results and conclusions at Sections 4 and 5 are referring to the cloud data.

2.3 Google Earth Engine cloud platform

Following the algorithm definition, the analysis at the study sites was carried out through Google Earth Engine, GEE (Gorelick et al., 2017), a cloud computing platform for processing satellite imagery and many kinds of geospatial and observation data. GEE comprehends a catalogue of satellite imagery and geospatial datasets of over twenty petabytes at planetary scale, together with the analysis capabilities needed to process them. The data are freely available for scientist, researcher and developers, who can access and process them through the Earth Engine API using both Javascript or Python. The development of Web-Application is also possible from the code editor interface. In this study, we developed a code to read, extract and analyze NIR data at the considered gauging stations.

3. Method

In this section, the original CM approach, as proposed by Tarpanelli et al. (2013) and subsequently modified by Tarpanelli et al. (2017), is described and adapted to the Sentinel-2 data. In particular, the higher spatial resolution with respect to previous studies allows to highlight two aspects that have been neglected so far: 1) the position of the M pixel, which might be different for low and high flows, and 2) the influence of suspended sediments on the C/M ratio and, thus, on the estimated river discharge. Based on the spatial-temporal behavior of the reflectance in the analyzed area, a modification of the original formulation is proposed, to take into account the presence of patterns and features resulting from the high spatial resolution images. The new formulation is implemented in the GEE platform for its extensive use.

3.1 Adaptation of the original CM approach to Sentinel-2 data

Following the previous study of Brakenridge et al. (2007) carried out with AMSR-E datasets, Tarpanelli et al. (2013) developed an approach to estimate river discharge from reflectance data based on the different responses of water and soil to radiation in the NIR band. Indeed, in this region of the electromagnetic spectrum, the reflectance of soil and vegetation is much greater than that of pure water. Therefore, the reflectance of a "wet" pixel, located near the boundaries of the river, changes according to the river discharge variations: specifically, it decreases when river discharge increases and the pixel is flooded. Changes in reflectances are not caused only by changes in river discharge, but could be also related to other sources, such as vegetation, atmosphere composition, soil moisture variations and bidirectional reflectance effects, not negligible over water bodies (Kremezi and Karathanassi, 2019). A "dry" pixel not affected by river discharge variation is then selected to correct the measure, assuming to be affected by the same sources of noise, as mentioned above. By defining the "dry" pixel as Calibration (C) pixel and the "wet" pixel as Measurement (M) pixel, it is possible to obtain a proxy of river discharge by calculating the NIR reflectance C/M ratio. An exponential filter (Wagner et al., 1999) is then applied to the ratio to reduce the effect of residual noises. The locations of C and M are generally calibrated by calculating all the possible combinations of the reflectance C/M ratio on a certain area in the vicinity of the gauged station and by comparing them with the in-situ measurements of river discharge, paying attention that no relevant source of water intake or outlet is located inside the selected region or between the latter and the gauged station. The reflectance ratio providing the highest correlation defines the best location for M and C (see Tarpanelli et al., 2013 for details).

The passage from medium to high spatial resolution images required several adjustments. The first one was related to the sensitivity to cloud of the NIR band. The solution adopted by Tarpanelli et al. (2013) for the medium resolution product consisted in discarding all the images affected by clouds. To make the procedure automatic, in this work, the Sentinel-2 images where the label "percentage of cloudy pixels" was greater than 70% were discarded because the residual valid pixels were not statistically sufficient to represent a robust sample. Moreover, the Sentinel-2 cloud probability product was used to mask each Sentinel-2 image's pixels with a probability greater than 50% of being cloudy. The choice of the threshold is based on the fact that for lower values (30-40%), the cloud detection algorithm may occasionally confuse water pixels as clouds in the selected areas, while some cloudy pixels could be confused as valid if higher thresholds were adopted (60-70%). Moreover, just for development purposes, a visual inspection of each NIR images provided by MEEO was carried out to verify the chosen threshold and to discard those in which the river was not clearly visible, i.e. in case of failure of the cloud detection algorithm or in case of few pixels to be used in the analysis.

The cloud masking has the side effect to replace clouds with "holes" of no-data in each image. Therefore, the selection of a single pixel for C, as in the original formulation, should be avoided in order to prevent the loss of data in case a cloud appears over the selected "dry" pixel. Following Tarpanelli et al. (2017), the C timeseries was defined as the average reflectance value of the pixels that had a low temporal coefficient of variation (specifically lower than 5^{th} percentile) with respect to all the pixels of the selected area.

Regarding the M pixel, as previously noticed, it should be selected over the river boundaries, since this area is the interface between water and soil and it is particularly sensitive to river discharge variations. The selection was constrained to an extended water mask that includes the river and a buffer around it. The European Commission's Joint Research Centre (JRC) Global Surface Water map (Pekel et al., 2016) "max_extent" was used to identify the river region, after the application of a 2-pixels buffer (60 m) applied to enlarge the resulting river area. To assess the best location for M, each pixel within this extended water mask was selected to calculate the C/M ratio (except the pixels already selected for the calculation of C, if any was included in the water mask) over the full available timeseries. Then, the exponential filter was applied, using a value of the filter T parameter equal to 5, which is the median number of days between two consecutive acquisitions of Sentinel-2 images. The Spearman correlation between the observed river discharge and the obtained filtered C/M series was then calculated, as shown in Figure 1b for Pontelagoscuro station. By comparing Figure 1a with Figure 1b, it is evident that the highest correlations for the M pixel coincide with the sediment deposit not vegetated near the river bank.

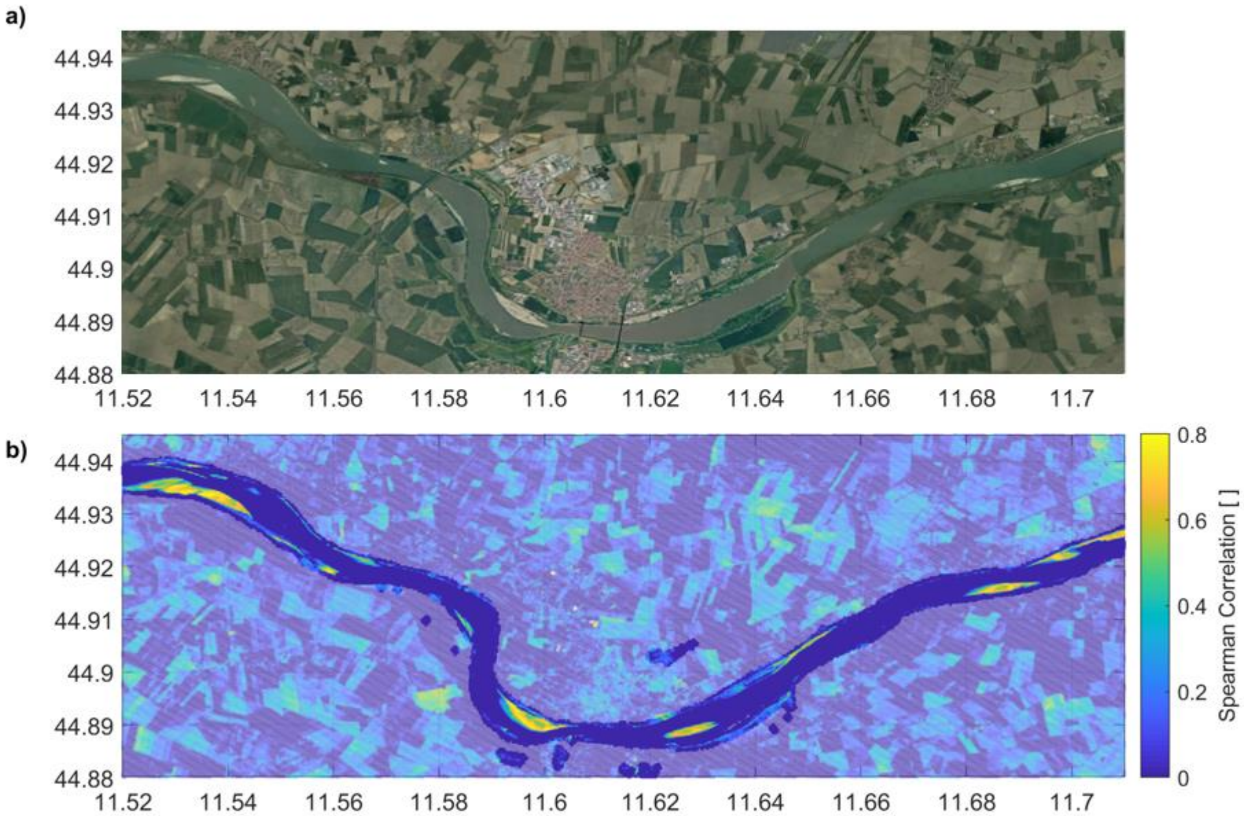

Figure 1: Po River at Pontelagoscuro station. Panel a) represents the location of the area from Google Earth (Copyright ©2021, CNES / Airbus, European Space Imaging, Landsat / Copernicus, Maxar Technologies). Panel b) shows Spearman correlation between filtered C/M and the ground observed river discharge, obtained varying the location of pixel M and fixing C as the average of the pixels with coefficient of variation lower than 5th percentile calculated between January 2018 - September 2019.

3.2 Limits of the CM approach for high resolution products

The expected benefits of the use of satellite imagery at high spatial resolution consist in the possibility to observe and account for aspects related to river discharge estimation that are not clearly observable from lower resolution products. In this paper, two main factors were considered to improve the CM approach: the presence of sediments in the water and the selection of multiple pixels for M. In order to better observe these phenomena, an analysis was carried out in a smaller area of the Po River at Pontelagoscuro (Figure 2a), within the coordinates [11.588 °E, 11.605 °E, 44.887 °N, 44.9 °N], in the period January 2018-September 2019.

The reflectance of clear water in the NIR band is very close to zero, but the reflectance of the river generally appears to be different from zero, although it remains low compared to soil or vegetation. During high flows, rainfall events mobilize large amounts of fine sediment into river systems (Keesstra et al., 2019), which contribute to the suspended sediment loads in the river, thus increasing the water reflectance (Ahn and Park., 2020). In these cases, the expected decrease in M reflectance due to inundation is hindered by the reflectance increase caused by the change in suspended sediments in the river. Consequently, the C/M ratio fails in estimating high flow, when the measure is most useful. This phenomenon is clearly visible in Figure 3a, where the hydrograph of the river discharge at Pontelagoscuro during the flood event of October-November 2018 is shown along with the C/M ratio calculated by selecting M as the single pixel that showed the highest Spearman correlation with the observed discharge (see the location of M in Figure 2b). By observation of two images acquired before and in concomitance with the flood event (Figure 3b-3c), the river becomes larger and strongly turbid, increasing its reflectance up to values very close to the surrounding soils (see Figure 3c). During and after the flood event, the suspended sediments decrease due to the catchment sediment dynamic (Keesstra et al., 2019; Gentile et al., 2010), which is different from the river discharge dynamic. Consequently, M decreases and the C/M ratio increases (see Figure 3a), leading to the late detecting of the inundation. In order to correct the issue, particularly important in the hydrograph rising limb, a correction should be introduced in the formulation of the CM approach to taking in account the role of the suspended sediments.

Another important aspect is strongly related to the pixel dimension of Sentinel-2. Due to the high frequency of the NIR electromagnetic waves and to the water absorption properties in this band, the NIR reflectance decreases significantly with water depth down to 0.75 m (shallow water condition, Gilvear et al., 2007) and remains constant for lower depths. A completely flooded pixel would therefore lose most of its sensitivity to the water level increasing and thus, to the river discharge variation. A single pixel of Sentinel-2 is too small to account for the variation of the river discharge over the study area because the width of the Po River during a flood event is much larger than the dimension of a single Sentinel-2 pixel (compare Figure 3c and 3b for the Po River width variation). Indeed, by looking at Figure 3a, the C/M ratio obtained from the maximum correlated pixel shows a limited variability during the low flow from July to October 2018, being the chosen M pixel located over completely dry soil. In the high-resolution product analysis, the single pixel can be affected by both long period of dry condition (with reflectance very similar to the soil) alternated with period of saturated conditions (completely flooded pixel, with reflectance very similar to the water inside the river). When the flow variation causes a pixel to be saturated, the relative C/M ratio stop varying and therefore the selected pixel cannot be used to properly represent further variation of river discharge.

This is confirmed by the location of the pixels showing the highest correlation coefficients with the ground observed river discharge: for medium-low flows (river discharge values below the threshold of 50th percentile, around 1000 m^3/s in the selected period), the highest Spearman correlations were obtained more internally into the river, as shown in Figure 2c. Conversely, the highest Spearman correlations were obtained in the external area (Figure 2d) for high flow condition (river discharge values above the threshold of 50th percentile). On the basis of these considerations, the choice of a single pixel for all river conditions is not advisable: M should be based on multiple pixels, chosen so as to take almost all the river regimes into account.

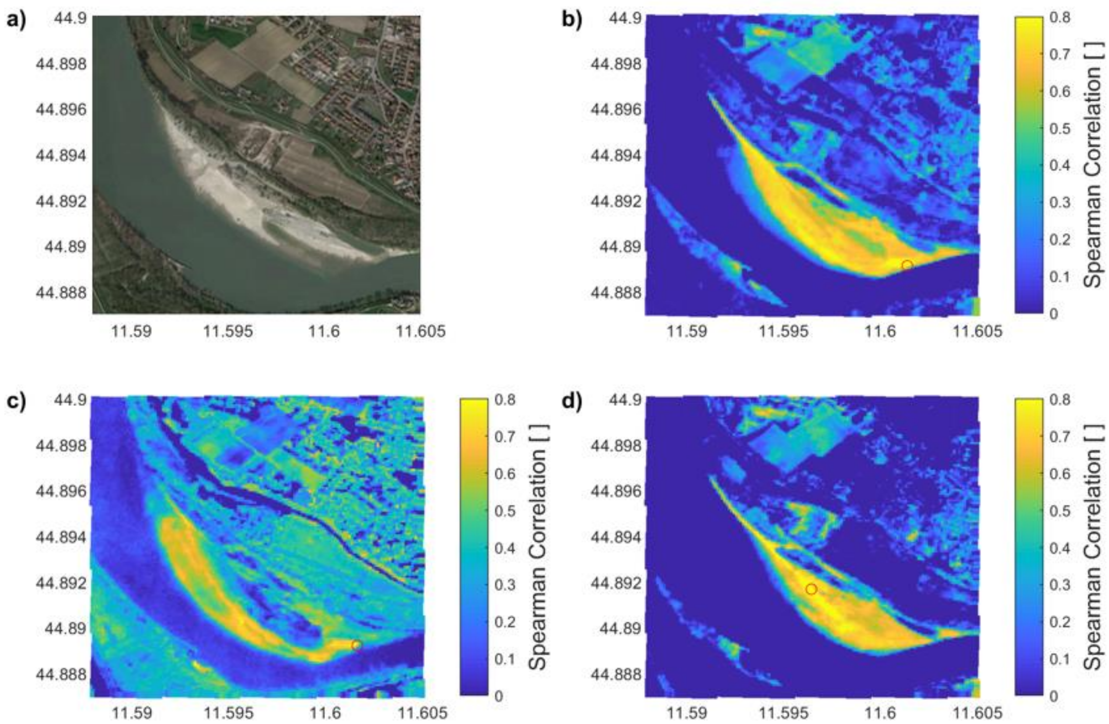

Figure 2: Po River at Pontelagoscuro station. Panel a) represents the area from Google Earth (Copyright ©2021 Immagini ©2021, CNES / Airbus, Maxar Technologies). Panels b), c) and d) show Spearman correlation between filtered C/M and the ground observed total discharge (b), low discharge below the 50th percentile (c), high discharge above the 50th percentile (d). The red circles in panels b, c, d represent the position of the M pixel where the Spearman correlation with the ground-based observations is highest.

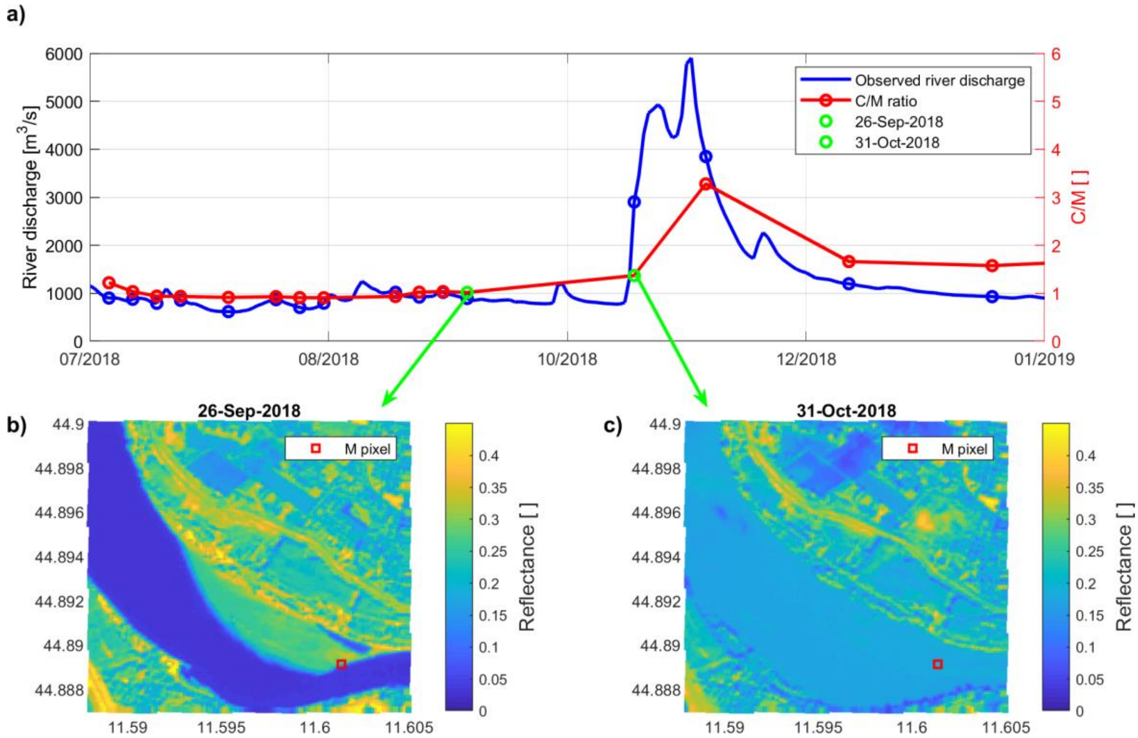

Figure 3: Po River at Pontelagoscuro station. Panel a) shows the hydrograph of the river discharge and the C/M ratio calculated for the analyzed area. The circles on the temporal series represent the days when the satellite overpasses. Panel b) and c) show the Sentinel-2 reflectance images before and during the October-November 2018 flood event, respectively. The red squares in the panels b and c represent the position of the M pixel, where the Spearman correlation with the ground-based observation is the highest.

3.3 A new formulation: the CMW approach

Following the considerations described in the previous paragraph, two main modifications of the CM approach are required: the management of suspended sediments effect and the use of multiple pixels for M selection.

The role of suspended sediments is important for a correct evaluation of the M reflectance. As specified above, the presence of suspended sediments makes the water turbid and increases the M reflectance, with the consequent decreasing of the C/M ratio especially during high flows. In order to evaluate the reflectance of the turbid water, it is necessary to average the reflectance of multiple water pixels, W, located over a region of the river constantly wet (inner part of the river, with water always present, also during low flows). Assuming W reflectance as a proxy of the presence of suspended sediments, M should vary between C for low flows (dry conditions) and W for high flows (wet conditions).

The original CM approach for the estimation of the river discharge, Q, assumed as:

$$Q \propto CM = \frac{C}{M} \tag{1}$$

can be then reformulated as:

$$\boldsymbol{Q} \propto CMW = \frac{\boldsymbol{C}}{\boldsymbol{M-W+z}} \tag{2}$$

where z is a numerical coefficient: in condition of high flow, M tends to be completely flooded and therefore its value is very close to the one of W. Any noise within their measurements can cause their difference being lower than 0, invalidating the obtained index. Furthermore, in case the selected M pixel become completely flooded, the condition of $M = W$ would be verified and the CMW ratio would tend to infinity. For both these reasons, we introduced z as

$$z = \max\,(W - M) + \min(M) \tag{3}$$

W pixels have to be selected within the river. This condition can be ensured by considering only the pixels included within a water mask, and by calculating, for each pixel, the product between the temporal average of the reflectance (the lower, the more probable presence of water) and its temporal standard deviation (the lower, the less variation occurs in the pixel). The W reflectance of eq. (2) can be then calculated by averaging the NIR reflectance of the pixels for which the product above defined is below a threshold (fixed at the 5th percentile according the sensitivity analysis, see Section 4.1), in order to identify the pixels where water is always present.

The timeseries of M should be obtained by averaging reflectances from multiple pixels located in an area within the water mask that is particularly sensitive to variations in river discharge. In this paper, we investigated several configurations to analyze the best strategy: 1) single pixel; 2) 3x3 pixels; 3) 9x9 pixels; 4) multiple pixels. In particular, configuration 1) was investigated to be compared to the original formulation. Configurations 2) and 3) were investigated to identify possible improvements from the evaluation of multiple pixels. Finally, configuration 4) was included in order to not calibrate the position of the M pixels with the ground observed discharge timeseries, but to approach an automated procedure for selecting an area or set of pixels that is particularly suitable for describing the river discharge variation. This area was identified following the fact that the NIR reflectance timeseries of the constituent pixels should not be correlated with the W and/or C timeseries. Specifically, pixels sensitive to low flow should be poorly correlated with C (because they are inundated most of the time), while those sensitive to high flow should be poorly correlated with W (because they are dry most of the time). Therefore, the condition that a pixel has to meet for being selected as one of the optimal M pixels is a very low Spearman correlation in reflectance with the pixels of W or C (lower than the 10^{th} percentile, according to the sensitivity analysis descripted in Section 4.1). In addition, to avoid selecting permanently flooded pixels (because they are poorly correlated with C), a maximum threshold on the pixels Spearman correlation with W is set to a fixed value (0.7 according the sensitivity analysis, see Section 4.1).

Summing up, the new procedure to estimate river discharge from high-resolution NIR reflectance data consists into the following steps (see also Figure 4):

1. The water mask is delineated through the “max extent” from JRC Global Surface Water map by considering a buffer of 3 pixels around each pixel of the water map;
2. each image where the field “percentage of cloudy pixels” of the Sentinel-2 product indicates a percentage of cloudy pixels greater than 70% is directly discarded and each image’s pixels in which the cloud probability is greater than 50% is masked out. Furthermore, the images with less than the 20% (empiric threshold) of valid pixels over the extended water mask are also discarded;
3. the C timeseries is calculated by averaging the reflectance of those pixels showing a temporal coefficient of variation lower than a certain threshold (5^{th} percentile, see Section 4.1);
4. the W timeseries is calculated by averaging the reflectance of those pixels, included in the water mask (step 3), whose product between temporal average and temporal standard deviation of reflectance values is below a certain threshold (5^{th} percentile, see Section 4.1);

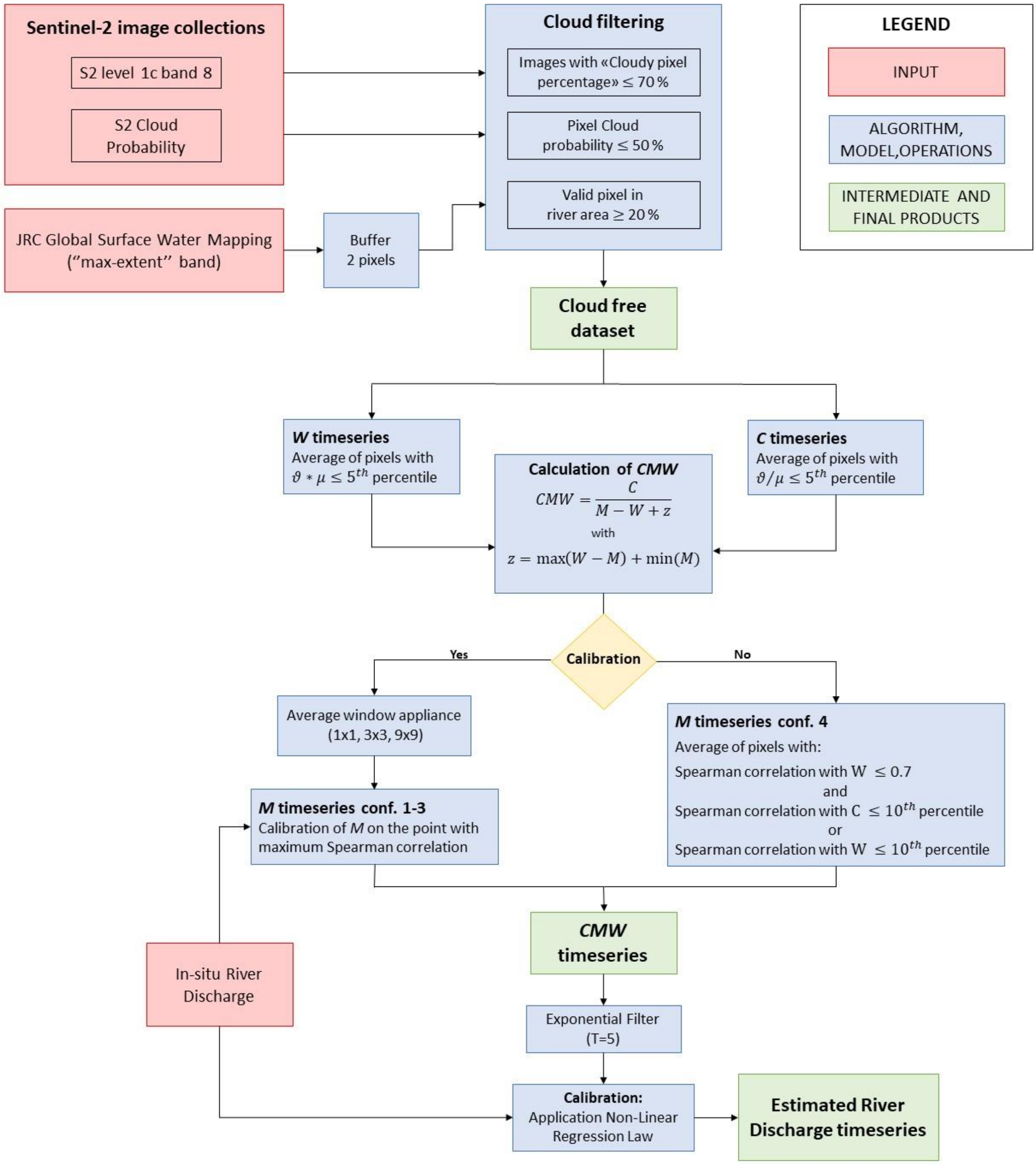

Figure 4: Flowchart of the CMW approach. The thresholds are identified according to the analysis shown in Section 4.1.

5. the M timeseries are obtained by considering the four configurations mentioned above. In the first three configurations, each pixel within the water mask (step 3) is used to calculate the ratio CMW according to eq. (2): in the case of configuration 2 and 3 each pixel value is resampled with a moving average spatial window of 3x3 pixels and 9x9 pixels, respectively. The pixel where the Spearman correlation between CMW

and the ground observed discharge is maximized, is selected as M pixel. Alternatively, for configuration 4, multiple pixels in the water mask having Spearman correlation with W or C below a percentile threshold (10^{th} percentile, see Section 4.1) and with W below a fixed value (0.7, see Section 4.1) are selected and averaged to obtain M without the use of any information from ground data (for this reason we referred to this configuration as uncalibrated).

6. C, W and M are used to calculate CMW index, which is then filtered through the exponential smoothing function with *T* equal to 5 days.

In order to compare the improvements of the new CMW approach, the CM approach was also tested, following the same steps except for the 4^{th}, because W was not needed, and replacing CMW index by C/M ratio in the step 5.

Both approaches were also tested using MODIS data, in order to compare the high with the medium spatial resolution data and evaluate potential benefits. The adopted procedure is very similar to the Sentinel-2 one, with the following exceptions:

1) a buffer of 3 pixels (instead of 2) is applied to the Global Surface Water map (Pekel et al., 2016) to identify the extended area over the Tiber River, since otherwise the water mask size could not reach the spatial resolution of MODIS pixels;
2) due to the absence of a MODIS Cloud Probability product in GEE, the cloud filtering is performed by exploiting the "state_1km" band of MYD09GA product. Specifically, all the pixels labelled as cloudy, mixed, cirrus, snow, ice or adjacent to cloud are masked out;
3) configurations 2 and 3 are not applied to MODIS data because a single pixel of this sensor exceed the sensitivity of a Sentinel-2 pixel in configuration 3 (~90x90 m of Sentinel-2 against ~250x250 m of MODIS).

3.4 Performance scores

In terms of performance scores, the coefficients of correlation of Spearman, *Rs*, and Pearson, *Rp*, were calculated between the CMW or CM timeseries and the ground observations of river discharge. Then, the estimation of the river discharge from CMW or CM was performed by a fitting function (cubic function) described, for CMW, as:

$$\tilde{Q} = a + b \cdot CMW + c \cdot (CMW + d)^3 \quad (4)$$

where $\tilde{Q}$ is the estimated river discharge, *a*, *b, c* and *d* are parameters, with *b* and *c* being positive so as to ensure the monotonicity of the function. The parameters were calibrated for each station using in-situ discharge observations in order to obtain the most accurate river discharge estimation.

Once the function was defined, three performance scores were computed to quantify the error in the final estimation of the river discharge: i) the Root Mean Square Error (*RMSE*), ii) the relative RMSE (*rRMSE*), defined as the ratio between *RMSE* and the mean observed river discharge and iii) the Nash-Sutcliffe efficiency (Nash and Sutcliffe, 1970), *NS*.

4. Results and discussions

This section contains the results obtained from the analyses of Sentinel-2 and MODIS data, carried out with the help of the Google Earth Engine, in the period: July 2015 – December 2020. First, the sensitivity analysis carried out on the thresholds selected to identify the masks for every configuration is shown for Pontelagoscuro station, along the Po River. Then, taking in account the selected thresholds, the approach is applied at Pontelagoscuro and Montemolino (Tiber River) stations and a deep analysis on the masks and the consequent results is carried out. Finally, the analysis is extended to the seven stations and the results are shown by comparing the original algorithm CM and the new formulation CMW for both the products Sentinel-2 and MODIS.

4.1 Sensitivity analysis

The methodology developed to infer the river discharge from NIR reflectance is based on the selection of multiple thresholds, needed to obtain the static masks of C, W and M. In order to assess the validity of the selected thresholds, a sensitivity analysis was conducted at the station of Pontelagoscuro. Regarding the calibrated configurations (1-3), the percentile thresholds to select C and W pixels was made to vary between the 2^{nd} and the 8^{th} percentile (1 percentile step), resulting in 21 possible layouts for the CM approach (7 C-masks * 3 calibrated configurations) and 147 possible layouts for the CMW approach (7 C-masks * 7 W-masks * 3 calibrated configurations). Regarding configuration 4, the thresholds related to the C and W masks selection were fixed at the 5^{th} percentile (based on the results of the other configurations) and just the ones related to the M selection were modified, to limit the degrees of freedom of the analysis. Therefore, the percentile correlation with C and W was made varied between the 8^{th} and the 12^{th} percentile (1 percentile step) and the maximum correlation with W between 0.5 and 0.9 with a (0.1 step), resulting in 125 different layouts (5 C percentile limits * 5 W percentile limits * 5 maximum correlation with W thresholds). The sensitivity of the thresholds was evaluated in terms of Spearman correlation *Rs* calculated between the obtained CM or CMW timeseries and the observed river discharge.

The sensitivity analysis was carried out for the station of Pontelagoscuro, where the methodology was developed. The obtained results in terms of Rs are shown in Figure 5. Regarding the calibrated approaches (configurations 1 to 3, Figure 5a and 5c), the selection of the percentiles for obtaining the C and W masks has little incidence on the performance of CM and CMW, varying the Rs in the range of 0.01. Based on these evidences, the percentile thresholds to select C and W pixels was selected equal to the 5th percentile, according to the work of Tarpanelli et al., 2017. The variability of configuration 4 results (Figures 5b and 5d) is instead in the order of 0.06 for CM approach and 0.03 for CMW approach, mostly ascribable to the threshold related to the maximum correlation with W. When the simple CM approach is considered (panel 5b) the high W correlation thresholds (dark red surfaces) allow to select many pixels in the inner river well correlated with W, providing worse performances with respect to the low thresholds (light red surfaces) due to the fact that these pixels are flooded most of the time and thus particularly sensitive to the sediment load of the river. This effect is worsened by choosing a low percentile correlation with W or an high percentile correlation with C: in both cases, the portions of pixels sensitive to low flows within M tends to be greater than those sensitive to high flows, obtaining the same aforementioned effect due to the absence of the sediment contribution within the CM. Conversely, if the CMW approach is applied (panel 5d), the presence of sediments is taken in account and accepting a larger number of pixels well correlated with W becomes advantageous for the final results. In the Pontelagoscuro area, positive effects on the results can be obtained also by increasing the percentile correlation thresholds of C and W, due to the presence of the vast area subjected to periodic floods noted in Figure 2. Notwithstanding this, such an area is not encountered in all the sections of a river nor in all the rivers. Therefore, the M mask selection thresholds for the configuration 4 were fixed at the 10th percentile for the correlation with W and C, whereas the maximum correlation with W was set at 0.7.

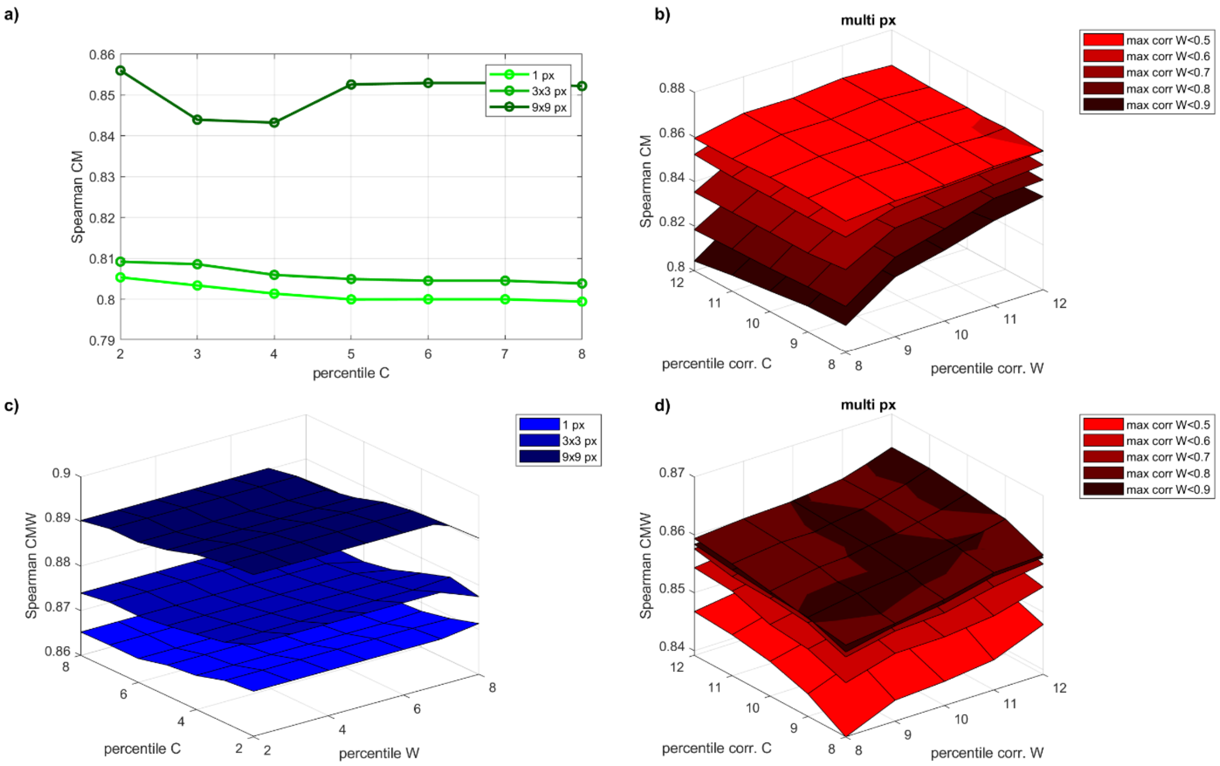

Figure 5: Sensitivity analysis at Pontelagoscuro station (Po River) in terms of Rs between CM and CMW timeseries and ground based river discharge. The subplots on the left show the Rs obtained using the CM (panel a) and CMW (panel c) approaches by varying the C mask from the 2^{th} to the 8^{th} percentile (panel a) and the C and W mask from 2^{th} to 8^{th} percentile (panel c) for the configurations 1 to 3 (indicated from light to dark green or blue). The subplots on the right show the Rs obtained by using the CM (panel b) and CMW (panel d) approaches for the uncalibrated configuration 4 where the correlation with C and W is made to vary between the 8^{th} and the 12^{th} percentile and the maximum correlation with W between 0.5 and 0.9.

4.2 Pontelagoscuro results assessment

Focusing on Pontelagoscuro station, a total of 743 images of Sentinel-2 Level 1C band 8 were available on GEE (accessed on 03/03/2022) during the period July 2015 – December 2020, obtained in 316 different days. After the cloud masking procedure, 168 cloud free images were retained and analyzed through the CM and the CMW procedure.

The timeseries obtained for the four configurations are shown in Figure 6, together with the hydrograph of the observed river discharge. All the configurations were successful in detecting the river dynamic. CMW approach showed a general better agreement with the observed discharge with compared to the CM approach, in particular at the beginning of the flood events in March 2016, May 2018, November 2018 and November 2019, when the high river discharge triggered a high level of sediment transportation. This can be noticed by observing the scatter plots on Figure 7, representing the CM and the CMW timeseries against the observed river discharge in green and red, respectively: most of the green dots in the upper-left area of the panels, characterized by low reflectance ratios and high discharge values due to the high sediment transportation condition, are avoided with CMW approach.

The results of the different configurations show that by increasing the number of pixels for the calculation of M (from the first to the fourth configuration, respectively on the top and the bottom of the Figure 6), CM approach improves, gradually agreeing with CMW approach with the exception of the aforementioned flood events. Indeed, by selecting a greater number of pixels, the reflectance ratio is more sensitive to river discharge variation, since each pixel becomes wet for different flow conditions and thus a greater variability of the ratio is obtained. Moreover, selecting a large area makes the approach less sensitive to residual sources of error, e.g., residual clouds and cloud shadows, since it is unlikely that all the M-mask selected area is equally affected by the noises.

Even though the new formulation is in good agreement with the observed river discharge and it improves the previous methodology, the peak floods experienced in November 2018 and November 2019 were still underestimated for all the configurations. This is due to the fact that the M pixels selected in the configurations were completely flooded for values of river discharge lower than those of the two peaks, preventing them to give information of flow events much greater than those at which they were saturated. Moreover, a registration issue between Sentinel-2 images was detected, leading to the impossibility of selecting precisely the river boundary pixels (additional details in Section 4.3). Indeed, the expected river width variation for very high flow is limited and the pixels sensitive to it are extremely few, due to the river embankments presence. The inaccuracy of Sentinel-2 imagery registration and the low frequency of highest discharge peaks (encountered just two times during the study period) meant that none of the pixels affected by them were selected by the M configurations. These flood events had in fact too low importance in terms of Spearman correlation to influence the pixels selection of the calibrated approaches and too low statistical significance to affect the one of the uncalibrated one.

It should be finally noticed that additional river discharge peaks were not detected due to the low temporal resolution of Sentinel-2 (no overpass during the flood events) and the discard of the images affected by clouds (gray peaks in Figure 6, e.g., see the flood event in December 2016). Notwithstanding this, the simulated discharges were in good agreement with the ground observed discharges, as confirmed by the performance indices of Table 1, that shows correlations *Rp* higher than 0.62 and *Rs* up to 0.89. If compared with the CM approach, *Rp* was higher than the CMW approach for all the configurations, with increments from +0.09 to +0.14. Similarly, improvements were observed by the use of multiple pixels rather than a single one, from +0.02 to +0.22 by considering both approaches together, in terms of Pearson correlation. Slighter improvements were also observed in terms of *Rs*. In terms of river discharge, by applying the cubic law of eq. 4, the performance scores of Table 1 show a decrease of *rRMSE* up to 0.19 and an increase of *NS* up to 0.45, considering both the multiple pixels and the different methodology.

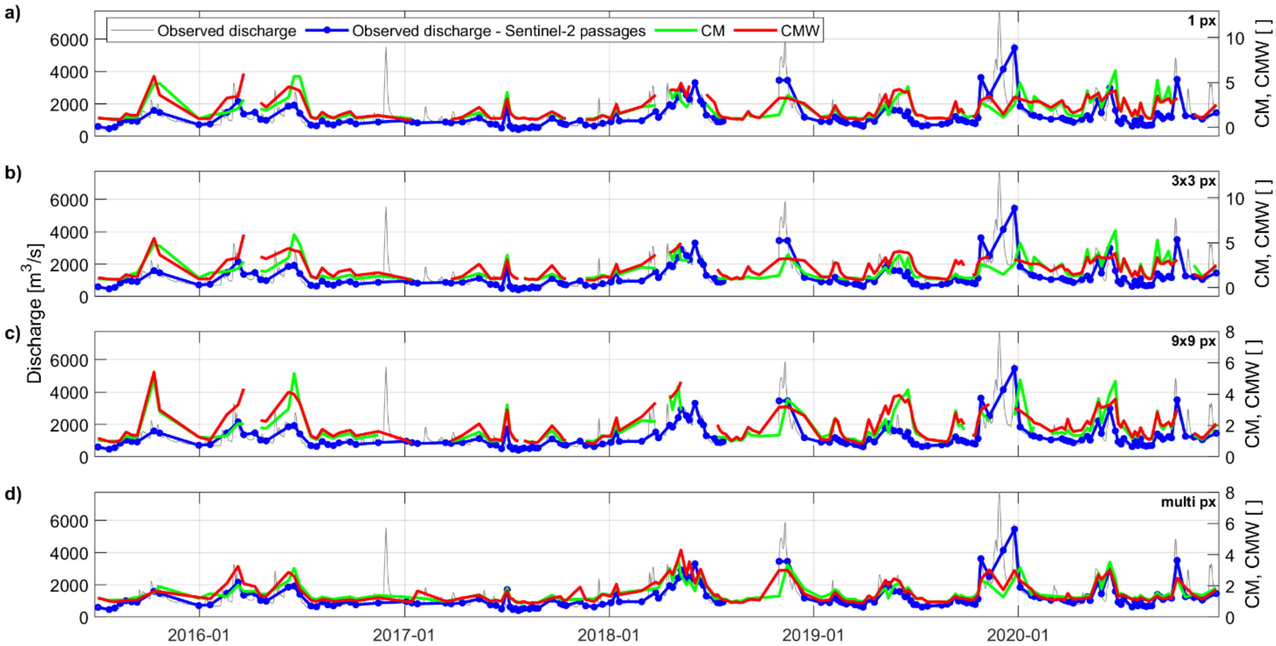

Figure 6: Po River at the Pontelagoscuro station: comparison in terms of temporal series between the ground observed discharge and the CM (green) or CMW (red) timeseries for configuration 1 (single pixel, panel a), configuration 2 (3x3 averaged pixel, panel b), configuration 3 (9x9 averaged pixel, panel c) and for configuration 4 (multiple uncalibrated pixels, panel d). The observed discharge is shown in light grey for the full timeseries and in blue for the measurements coincident to Sentinel-2 overpass.

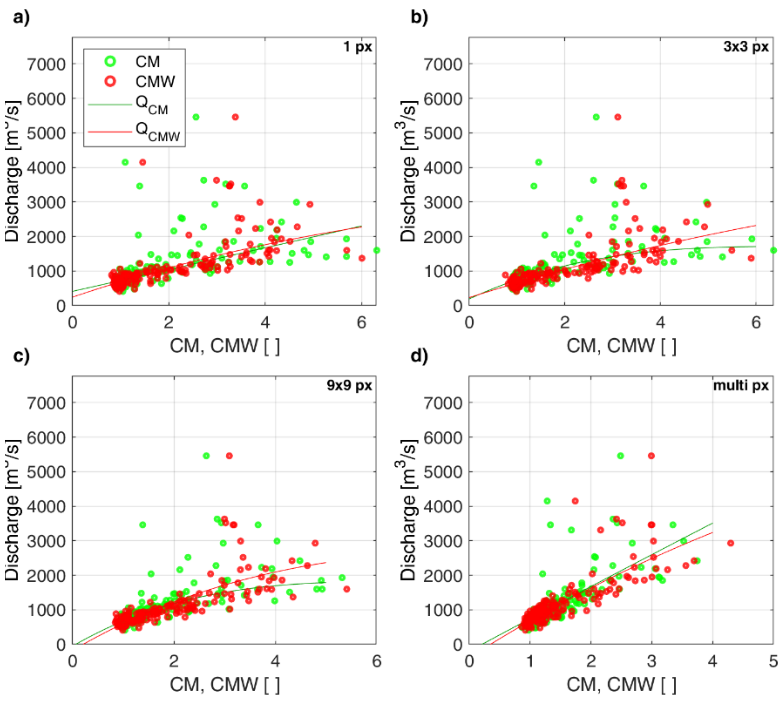

Figure 7: Po River at the Pontelagoscuro station: comparison in terms of scatter plots between the ground observed discharge and the CM (green) or CMW (red) timeseries for configuration 1 (single pixel, panel a), configuration 2 (3x3 averaged pixel, panel b), configuration 3 (9x9 averaged pixel, panel c) and for configuration 4 (multiple uncalibrated pixels, panel d). The calibrated relationships of the estimated river discharge are shown as solid lines for both CM (dark green) and CMW (red).

Table 1: Performance scores for the different configurations (1 for single pixel, 2 for 3x3 pixels, 3 for 9x9 pixels and 4 for multiple pixels) for the period 2015-2020 at Pontelagoscuro station. Spearman (Rs) and Pearson (Rp) correlations are calculated between the CMW or CM timeseries and the ground observed river discharge. Root Mean Square Error (RMSE), relative Root Mean Square Error

(rRMSE) and Nash-Sutcliffe efficiency (NS) refer to the comparison between the simulated discharge calculated according eq. 4 and the ground observed discharges.

Config.	$\boldsymbol{CM}$					$\boldsymbol{CMW}$				
	Rs	*Rp*	*RMSE*	*rRMSE*	*NS*	*Rs*	*Rp*	*RMSE*	*rRMSE*	*NS*
	[-]	[-]	[m^3/s]	[-]	[-]	[-]	[-]	[m^3/s]	[-]	[-]
1	0.80	0.48	689	0.57	0.17	0.87	0.62	600	0.50	0.38
2	0.80	0.53	655	0.54	0.26	0.88	0.64	556	0.47	0.40
3	0.85	0.61	581	0.49	0.35	0.89	0.70	508	0.43	0.50
4	0.85	0.70	545	0.45	0.48	0.86	0.79	461	0.38	0.63

By moving from the single to aggregated pixels, the performance increased, reaching the best values for configuration 4. This is justified by the Sentinel-2's pixels size, which is smaller than the Po River width: it is convenient to aggregate multiple pixels for a proper representation of the river discharge.

Figure 8a shows the pixels of the box with lower (less than 5th percentile) temporal coefficient of variation, selected to obtain the C timeseries. As expected, they are mostly concentrated over roads and bare soil areas, due to the temporal stability of the reflectances measured in these areas. Figure 8b shows the pixels within the water mask selected for the W timeseries. They represent the lower (less than 5th percentile) product between the average reflectance and its standard deviation, represented in Figure 8d, and they are correctly identified in the center of the river. Figure 8c represents the selected M pixels: the different calibrated configurations (1-3) are highlighted with different colors, while the light grey area shows the M pixels selected by the configuration 4 (without using any ground observation for calibration) and coming from the evaluation of the Spearman correlation between the reflectance timeseries of each pixel included in the water mask (except those pixels already used for W and C) and the timeseries already calculated for C (or W) deriving from the masks in Figure 8e (or 8f). Specifically, the blue pixels in Figure 8e are poorly correlated with C, and coincide with those showing greater correlation with low flow (compare with Figure 2c) and those always inside the water. Conversely, the pixels in yellow in Figure 8f are highly correlated with W timeseries (stable water pixels) and therefore identify the inner river, while the blue pixels coincide with those showing greater correlation the high flow (compare with Figure 2d). Permanently flooded pixels (highly correlated with W) are also poorly correlated with C (Figure 8e), therefore the condition of Spearman correlation with W < 0.7 was needed to avoid their selection for the M-mask in configuration 4. This condition helps reaching a tradeoff between keeping low the number of pixels selected for M and ensure the sensitivity of the procedure to the high river discharge. In fact, the pixels sensitive to high flow condition are expected to be less in number than those sensitive to low flow condition due to the nature of the phenomenon: therefore, it is important to limit the selection of the pixels poorly correlated with C, sensitive to low flow, in order to balance the M pixels distribution. Despite this step, the M-mask obtained by configuration 4 is much larger than those obtained by configurations 1-3. However, this allows to decrease the sensitivity of M to atmospheric noises, by diluting the pixels affected by random clouds with a larger number of pixels.

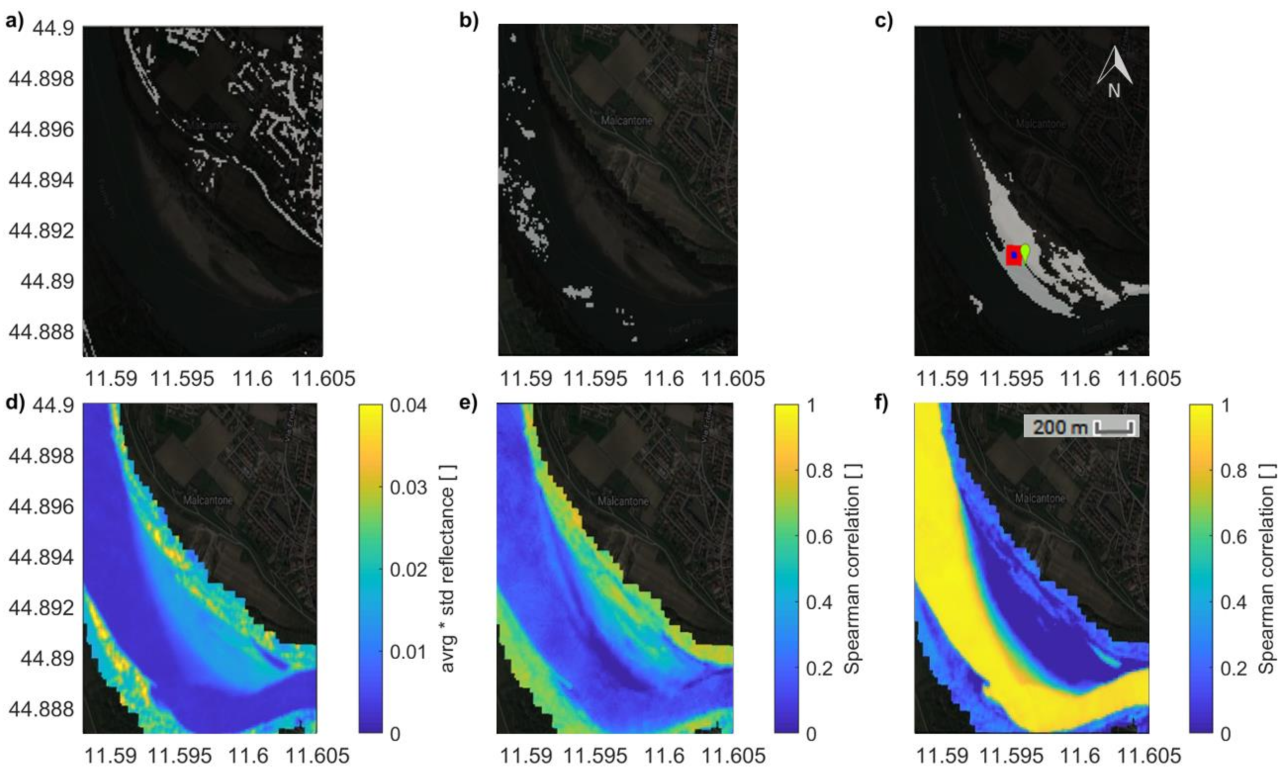

Figure 8: Po River at Pontelagoscuro: in light gray the pixels used for calculating C (panel a), W (panel b). Panel c shows the location of the pixel M obtained from configuration 1 (1 pixel, greed dot), configuration 2 (3x3 pixels, blue square), configuration 3 (9x9 pixels, red square) and configuration 4 (multiple uncalibrated pixels, light gray). Panel d) shows the product between the average and standard deviation of the NIR reflectance for each pixel within the water mask; panel e) and f) represent the Spearman correlation map between the reflectance timeseries of each pixel in the water mask and the average reflectance calculated for the C (panel e) and W timeseries (panel f), respectively. Background Copyright ©2021 Immagini ©2021, CNES / Airbus, Maxar Technologies.

In order to better asses the source of errors in terms of river discharge, we analyzed the Sentinel-2 images acquired during the days in which the difference between estimated and observed river discharge was the highest. One of the main disagreement reasons is the clouds presence. Despite the Sentinel-2 cloud probability mask allows to remove the majority of the them, some residual clouds were undetected and unmasked. Furthermore, cloud shadows were not considered in the masking process, and the pixels affected by those were not removed. Clouds are very bright in the NIR, therefore their presence cause river discharge overestimation when they overlap with C or W and underestimation when they coincide with M pixels. In contrast, cloud shadows reduce the reflectance of the affected pixels, causing underestimations when they coincide with C or W and overestimations when they overlap with M. An example of these issues is shown in Figure 9. The panels a and c show the Sentinel-2 1c band 8 image collected on 24/05/2018 over Pontelagoscuro area, before and after the application of the cloud probability mask at 50%. Residual clouds can be clearly distinguished over the river, while a cloud shadow is clearly distinguishable in the top of the figure. Panel b and d of Figure 9 show the image collected on 10/06/2017: few clouds were present on the west area of the river, but the algorithm masked out a large number of pixels that were confused with clouds, hampering the river discharge estimation. This is another source of noise cloud-related: in some cases, the mask fails in correctly identifying the clouds, filtering out valid pixels.

Another issue is related to the reflectance values of C. It was noticed that the reflectance values of the terrain pixels were occasionally significantly lower/higher than in other days, potentially due to, e.g., the effect of soil moisture variations or bidirectional reflectance effects. These conditions led to a lower/higher C value, which caused the under/overestimation of CMW and consequently of the flow peaks, worsening the effect of the pixels' saturation. This is the case for the floods occurred at the ends of 2020 (Figure 6), where CM and CMW index underestimated the river discharge due to a low value of C, causing most of the CMW outliers that can be noticed in Figure 7. Finally, it should be noticed that the fitting functions shown in Figure 7 were supposed to exhibit steeper behavior to compensate the effect of the M pixels saturation. The presence of residual clouds and shadow, however, generated outliers that compromised the effectiveness of the relationship, highlighting the need to improve the masking procedure.

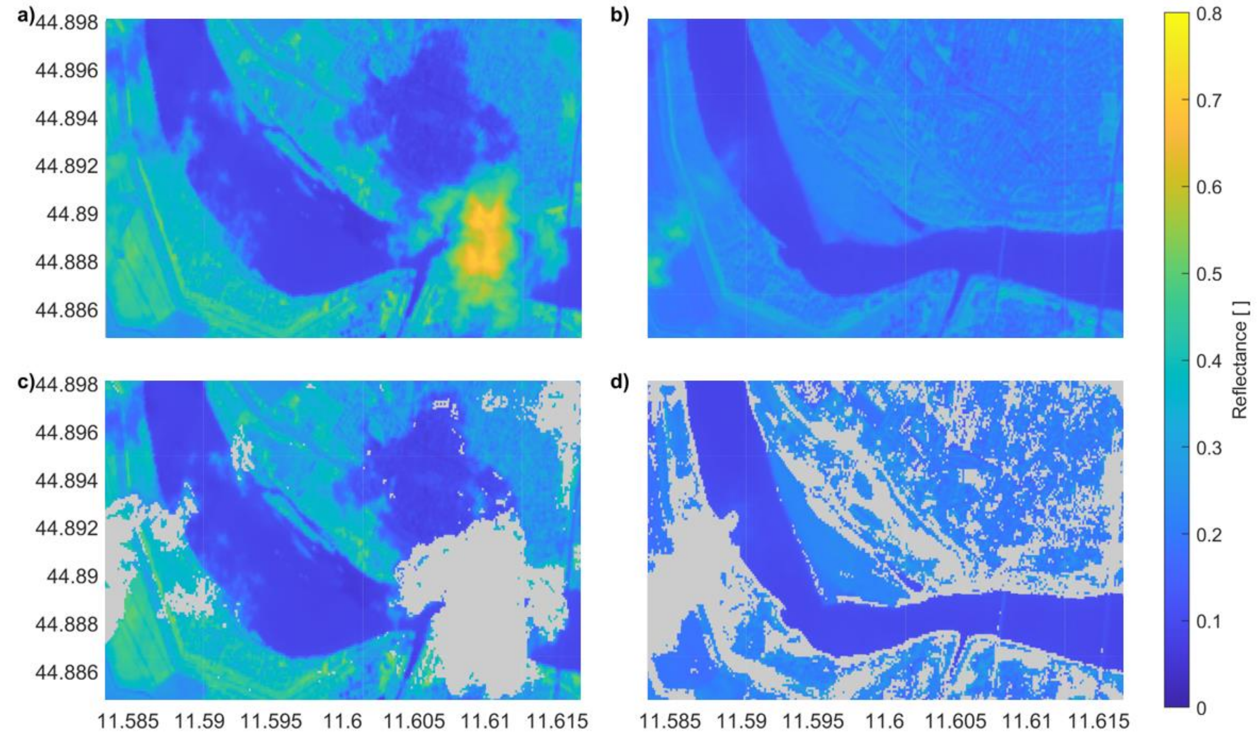

Figure 9: Po River at Pontelagoscuro: Sentinel-2 1c Band 8 images acquired on 24/05/2018 (Panel a and c) and on 06/10/2017 (Panel b-d), prior (a and b) and after (c and d) the application of the cloud mask equal or above 50% of cloud probability (light gray area).

4.3 Montemolino results assessment

The results obtained at Montemolino station, over the Tiber River, are described in this section. For this area the total number of available images for the period 2015-2020 was 728, obtained in 625 different days. After the cloud masking, 373 images with valid data were analyzed (based on the access on 03/03/2022).

Figure 10 shows the pixels selected from each mask at the Montemolino station over the Tiber River. As for Pontelagoscuro station, C-mask (Figure 10a) coincided with roads, parking and bare soil. The river bed was again successfully identified by the product of the average reflectance and its standard deviation (Figure 10d). The holes within the river course were caused by river zones that were not detected from the JRC Global Surface water map. In Figure 10b, the pixels selected for W were shown. It can be noticed that they did not fall within the center of the river but prevalently on its southern borders. A possible cause of this phenomena is the shadow created by the riparian vegetation, which decreases the average reflectance of the pixels affected by it and facilitates their selection. Figures 10e and 10f show the Spearman correlation between the reflectance timeseries of each pixel in the water mask and the C and W timeseries, respectively. Figure 10e shows many pixels poorly correlated with C over the northern river boundaries of the southern river branch, which were selected to obtain M timeseries by the uncalibrated configuration, as shown in Figure 10c. In contrast with the results obtained at Pontelagoscuro, by comparing Figure 10e with Figure 10f, it can be noticed that many of these pixels show a low correlation with W as well, while for the Po River the pixels poorly correlated with C were better correlated with W and vice versa. By further analyzing the selected area, a failure of the image co-registration procedure was detected: the coordinates of each image often not correspond to the real coordinates of the area, but there was often a misregistration of a few pixels. An example of this issue is shown in Figure 11, where the Sentinel-2 1c band 8 image acquired on 22/08/2017 is shown in panel a along with a clipping of the image acquired on 27/08/2017 in panel b: a miss-registration of ~1-2 pixels can be noticed by comparing the two images.

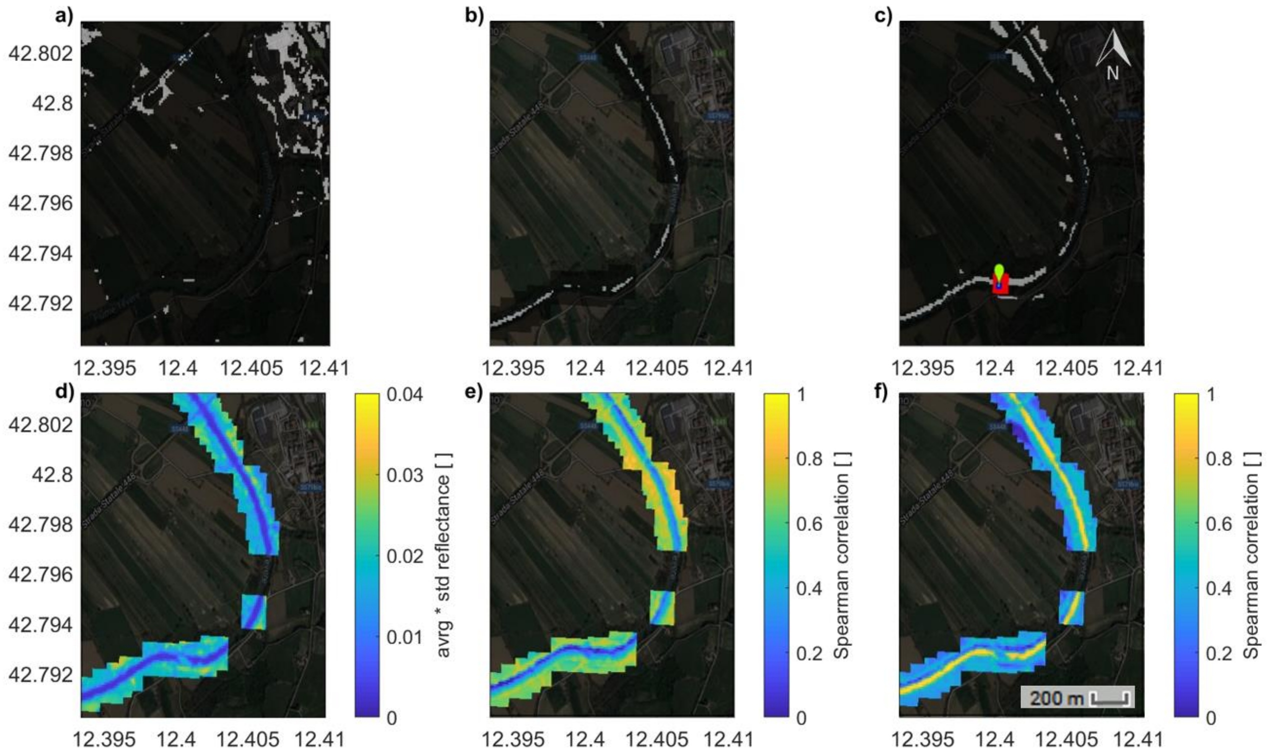

Figure 10: Tiber River at Montemolino: in light gray the pixels used for calculating C (panel a), W (panel b). Panel c shows the location of the pixel M obtained from configuration 1 (1 pixel, greed dot), configuration 2 (3x3 pixels, blue square), configuration 3 (9x9 pixels, red square) and configuration 4 (multiple uncalibrated pixels, light gray). Panel d) shows the product between the average and standard deviation of the NIR reflectance for each pixel within the water mask; panel e) and f) represent the Spearman correlation map between the reflectance timeseries of each pixel in the water mask and the average reflectance calculated for the C (panel e) and W timeseries (panel f), respectively. Background Copyright ©2021 Immagini ©2021, CNES / Airbus, European Space Imaging, Maxar Technologies.

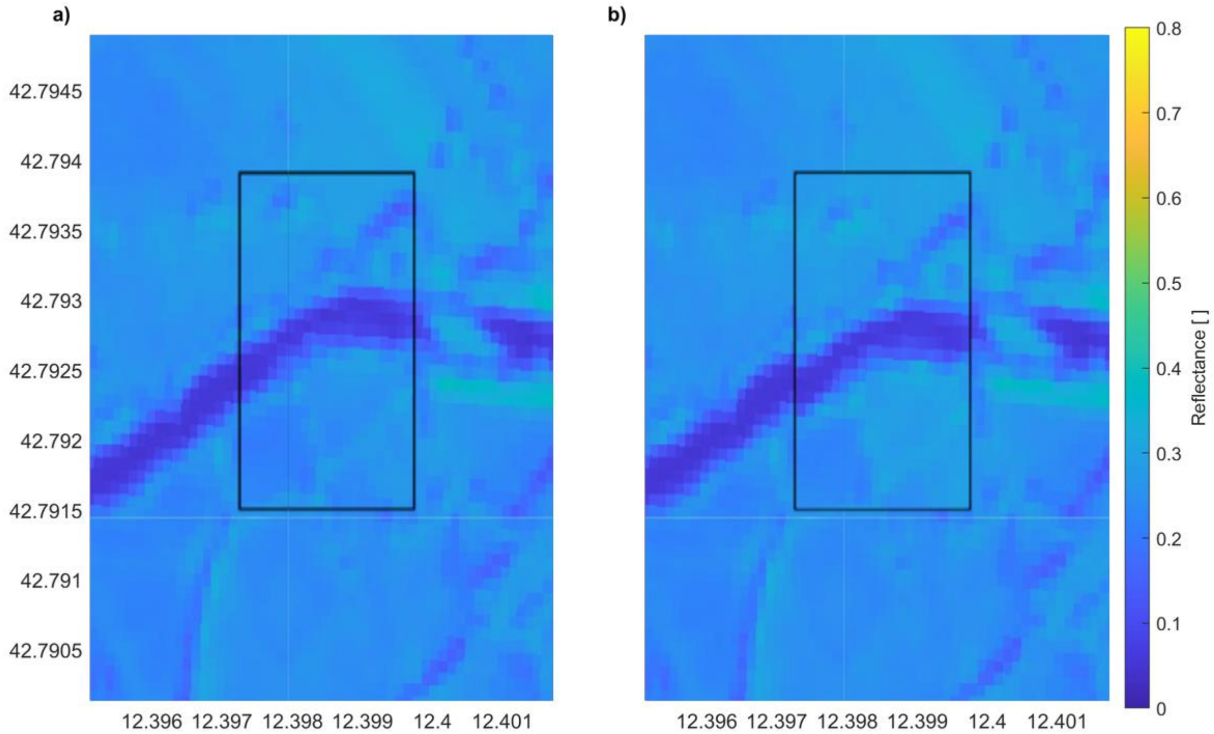

Figure 5: Tiber River at Montemolino: detail of Sentinel-2 1c Band 8 image acquired on 22/08/2017 (Panel a and b) and on 27/08/2017 (central patch Panel b), showing a miss-registration between the two images of about 1-2 pixels.

This apparent movement of the full river section caused many pixels vary "artificially" between soil and water, which were in turn selected for M from the automated procedure of configuration 4, even being insensitive to river discharge. The error was also found in Pontelagoscuro images, but it was less severe due to the different extent of the river, even if it can be responsible of the missing information for the greater river discharge peaks, since, as mentioned above, those are related to very few pixels. To correct the issue, several attempts were done using GEE *"register"* function without satisfying results, mainly because of the presence of geometric distortions between the analyzed Sentinel-2 images. The correction of this effect should be therefore entrusted to the data provider, in order to increase the multi-temporal consistency of Sentinel-2 dataset.

The M pixels chosen over the fields, in the north of Figure 10c, highlight two additional limitations of the automatic procedure. First, the vegetated pixels, which are poorly correlated with both C and W, are not taken in account by the configuration 4, and can be potentially wrongly selected for M . Second, the number of pixels sensitive to river discharge variation can change to not only rivers but also sections of the river itself. The use of the percentile to obtain M pixels is needed for the portability of the methodology between rivers of different sizes, but it could lead to select too many of them, especially for rivers with rectangular sections or narrow flooded area. In Montemolino case, for example, the most sensitive area is actually narrow and can be easily identified by looking at the M pixels selected by the calibrated procedures (configurations 1-3: green dot, blue area and red area, respectively, in Figure 10c): they fall in the same area inside the river, which is periodically submerged (it is shown in light blue color in Figure 10d: in some periods it dries, therefore the average reflectance and the standard deviation are higher with respect to the rest of the river area) and it is therefore sensitive to river discharge variation. No further sensitive areas can be clearly distinguished, probably due to the presence of the riparian vegetation, which obstruct their detection.

Once the C-, W- and M-mask were obtained, the C and W timeseries were used to estimate the river discharge with the CMW and the CM approaches, using both the uncalibrated and calibrated M timeseries. The performances of the obtained approaches for the river discharge estimation are shown in Table 2. The misregistration issue affects particularly the uncalibrated procedure, which showed the lowest performance in terms of *Rs*, *Rp*, *RMSE* and *NS*. The calibrated methods were also affected, with score values worse than those obtained at Pontelagoscuro. Neverthless, the relevance of considering sediment transport was again confirmed by the stable improvement in performances comparing the CMW and the CM results. Regarding the CMW approach, the configurations that show the best performance were the first two, where just one pixel and an area of 3x3 pixels were considered. This was due to the moderate width of the river, which requires a limited number of pixels to obtain the full river discharge variation.

Table 2: Performance scores for the different configurations (1 for single pixel, 2 for 3x3 pixels, 3 for 9x9 pixels and 4 for multiple pixels) for the period 2015-2020 at Montemolino station. Spearman (Rs) and Pearson (Rp) correlations are calculated between the CMW or CM timeseries and the ground observed river discharge. Root Mean Square Error (RMSE), relative Root Mean Square Error (rRMSE) and Nash-Sutcliffe efficiency, NS, refer to the simulated discharge calculated according eq. 4 and the ground observed discharges.

	$\boldsymbol{CM}$	$\boldsymbol{CMW}$

Config.	*Rs* [-]	*Rp* [-]	*RMSE* [m^3/s]	*rRMSE* [-]	*NS* [-]	*Rs* [-]	*Rp* [-]	*RMSE* [m^3/s]	*rRMSE* [-]	*NS* [-]
1	0.87	0.46	26.79	1.59	0.15	0.91	0.63	24.09	1.43	0.32
2	0.86	0.43	27.29	1.62	0.12	0.91	0.62	23.01	1.37	0.38
3	0.76	0.40	27.24	1.64	0.12	0.82	0.44	25.88	1.54	0.21
4	0.44	0.27	29.56	1.70	0.07	0.57	0.36	27.37	1.58	0.20

Figure 12 shows the timeseries of the ground observed discharge and those derived by CMW and CM approaches at Montemolino station for all the configurations. The quality of the uncalibrated procedure (Figure 12d) is relatively poor: even if flood periods were correctly detected, the surplus of M pixels and the registration issue of Sentinel-2 data deteriorates the information. The calibrated procedure shows instead better results (Figures 12a, b, c), even if all the river discharge peaks were underestimated, probably due to saturation issues. Low flow conditions were quite well represented in most configurations. These results are confirmed by the scatter plot shown in Figure 13: the configurations 1 and 2 (panel a and b) show a less sparse couples with respect of the configuration 3 and 4 (panel c and d), which suffer from great noises. This is also confirmed by the behavior of the fitting functions shown in the scatter plots, particularly for the CMW ones (red lines, Figure 13): those in panel a and b show the steep behavior expected due to the saturation of the M pixels, while the noises of configuration 3 and 4 (panel c and d) cause the obtained relationships to display a milder slope.

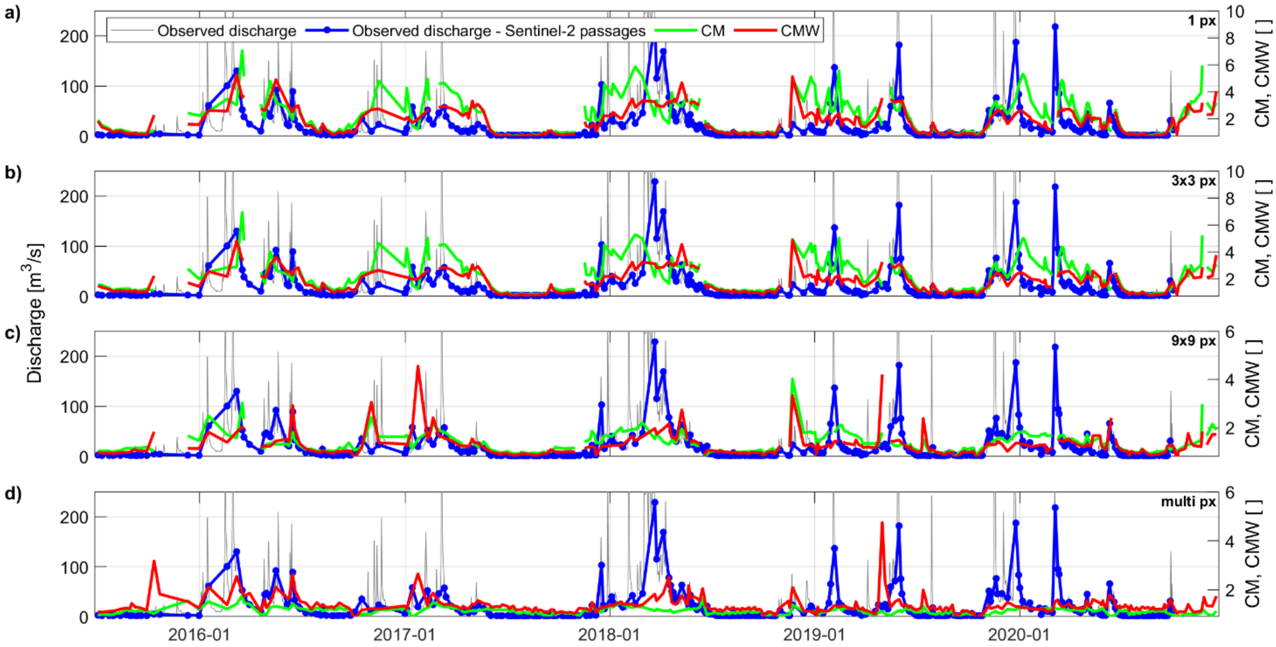

Figure 12: Tiber River at the Montemolino station: comparison in terms of temporal series between the ground observed discharge and the CM (green) or CMW (red) timeseries for the configuration 1 (single pixel, panel a), configuration 2 (3x3 averaged pixel, panel b), configuration 3 (9x9 averaged pixel, panel c) and for configuration 4 (multiple uncalibrated pixels, panel d). The observed discharge is shown in light grey for the full timeseries and in blue for the measurements coincident to Sentinel-2 overpass.

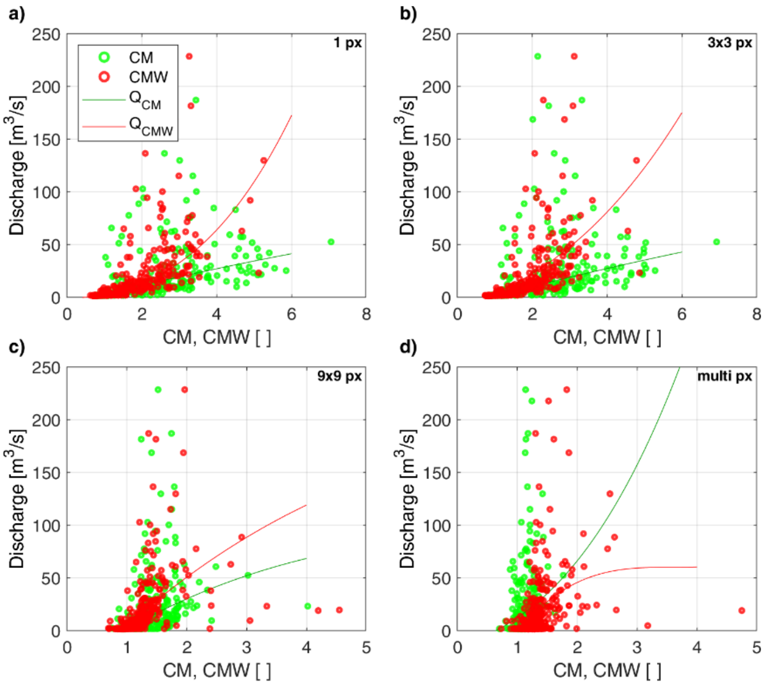

Figure 63: Tiber River at the Montemolino station: comparison in terms of scatter plots between the ground observed discharge and the CM (green) or CMW (red) timeseries for configuration 1 (single pixel, panel a), configuration 2 (3x3 averaged pixel, panel b), configuration 3 (9x9 averaged pixel, panel c) and for configuration 4 (multiple uncalibrated pixels, panel d). The calibrated relationships of the estimated river discharge are shown as solid lines for both CM (dark green) and CMW (red).

4.4 Comparison between Sentinel-2 and MODIS: overall results assessment

After the confirmation of the thresholds adopted and the acceptability of the results for both sites of Pontelagoscuro and Montemolino, the CM and CMW approaches were applied also to the remaining five sites by using data from both Sentinel-2 and MODIS. For Sentinel-2 all the configurations were considered, whereas with MODIS data only configurations 1 and 4 were adopted, because, in the configurations 2 and 3, the final size of the resampled MODIS pixel is too large to represent accurately the river and to apply the approaches with reasonable results. The performance indices obtained between the CM and CMW ratios and the ground measurements of river discharge at all the seven sites are shown in Figure 14.

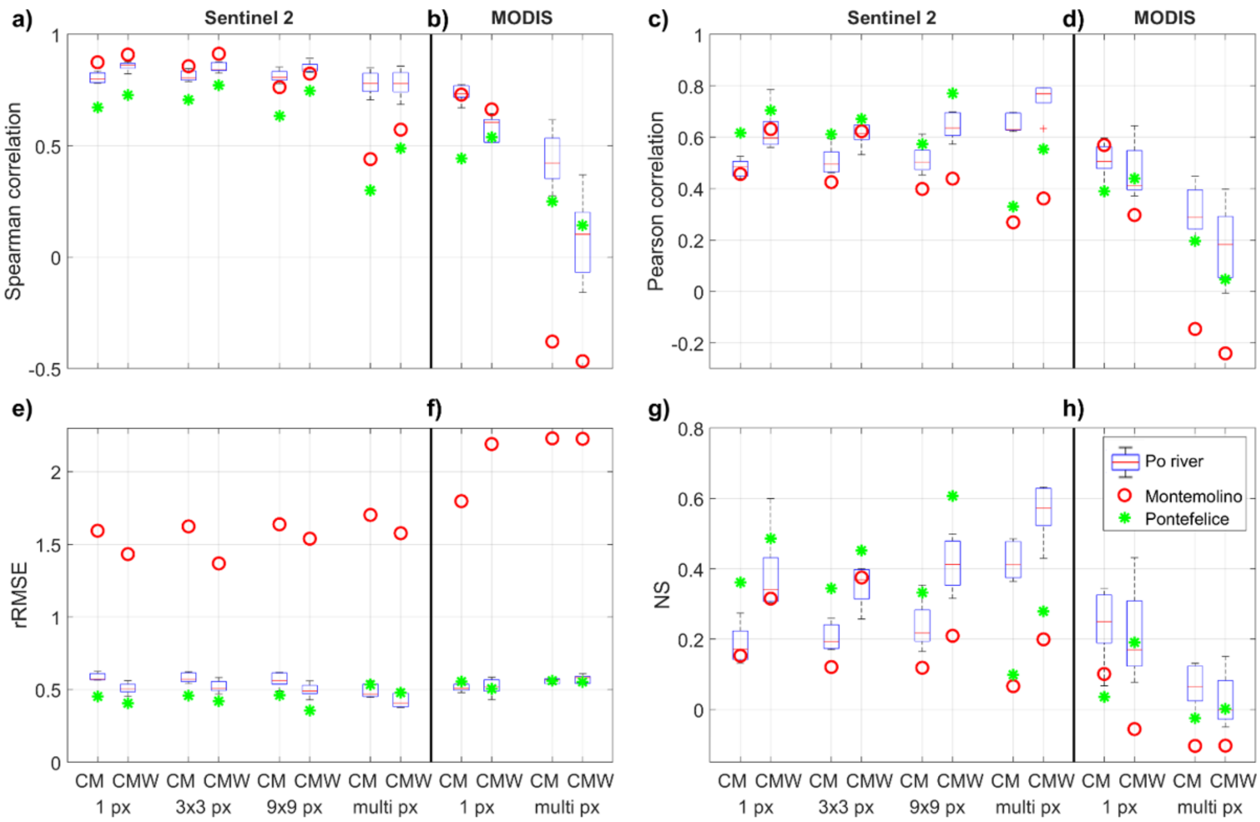

Figure 74: Spearman correlation, Rs (a, b), Pearson correlation Rp (c, d) between CM and CMW timeseries and ground observed discharges, relative Root Mean Square Error, rRMSE (e, f) and Nash Sutcliffe efficiency, NS (g, h) between estimated and ground observed discharges by using Sentinel-2 (a, c, e, g) and MODIS (b, d, f, h) data as input for the different configurations. For the five sites of the Po River, the results are represented with box plots, whereas with stars and circles for the two stations of the Tiber River.

The CM approach showed always lower or at most equal value of Rs or Rp compared to those obtained from the CMW approach when Sentinel-2 data were considered. Conversely, if MODIS data were adopted, CM had higher correlations than CMW (It should be noticed that the obtained results are lower than those of Tarpanelli et al. (2013;2020) because of differences in the adopted methodology, e.g., cloud masking, temporal interpolation). This was mainly due to the complexity in the selection of the W pixels in the latter approach when MODIS data are adopted. In fact, because its spatial resolution was similar to or bigger than the average width of the selected rivers, for low flows, the W pixels can be contaminated by a land fraction, adding a source of noise to the obtained CMW index and causing a loss in performance with respect to the original CM approach. Similarly, in the configuration 4, M is represented by the pixels that show low correlations with both water and soil, but since W signal was contaminated, the selection of M pixels was not optimal and consequently the performances were low. Moreover, the low spatial resolution of MODIS causes the existence of many mixed pixels composed by fractions of terrain, water and vegetation, whose signals will be poorly correlated with both C and W and thus erroneously selected for M. These considerations were particularly exacerbated at the Tiber River sites, where the width of the river was extensively lower than the MODIS resolution. Configuration 4 showed good results when Sentinel-2 data were used, with *Rs* similar to those obtained for the other configurations whereas *Rp* higher for the Po River. Slight worse performances were obtained for the Tiber River for both *Rs* and *Rp*. Specifically, the performances obtained by configuration 4 at the Tiber River were affected by the presence of the riparian vegetation and various agricultural fields in the neighboring of the river, together with the Sentinel-2 images registration issue as detailed in the Section 4.3.

Many of the considerations made for the correlations are confirmed for the performances of *NS* and *rRMSE* for the Po River. Instead, for the Tiber River the results at the two sites were very different each other. Montemolino showed very low performances, particularly in terms of rRMSE, mainly due to the registration issues of the Sentinel-2 images as discussed above. It is worth to notice that, despite the indices derived for the configuration 4 did not take in account any in-situ data in the calibration of C, M and W location, the knowledge of the ground observed discharge is still necessary to calibrate the parameters of eq. 4. Notwithstanding this, the obtained results are promising and represent a step forward towards the developing of a completely uncalibrated procedure to estimate river discharge from satellite data.

4.5 Discussion: potential and limitations

The application of the CM approach to Sentinel-2 NIR data allows enlarging its field of application to medium-small rivers, due to the higher spatial resolution of Sentinel-2 with respect to MODIS data, for which the approach was developed. The analysis of very narrow rivers (10-20 meters) is still challenging due to the presence of a co-registration issue among Sentinel-2 images. This issue has a strong impact on the obtained performances (as observed at Montemolino station, section 4.3), since it causes many pixels to vary "artificially" between soil and water, preventing the observation of the actual temporal variability of the selected pixels reflectance signals. Moreover, it should be noticed that the application of the sediment correction introduced in this study (CMW approach) to such narrow rivers should be avoided when Sentinel-2 imagery are used. In fact, when the average river width is close to the size of a Sentinel-2 pixel, the probability that W pixels are contaminated by soil increases, thus adding a source of noise that affects the obtained performances. The same effect has been observed from the application of the CMW approach to MODIS data over the Po River (Section 4.4): the average Po River width at Pontelagoscuro (~300 m) is close to the size of a MODIS pixel (~250 m), so the selected W pixels are contamined by soil and do not reflect the actual variability of the water reflectance. The sediment correction is therefore biased, and the CMW approach is less performing than the original CM approach.

Notwithstanding these technological limitations, this study successfully demonstrated that high spatial resolution and sediment correction allow to increase our ability to estimate river discharge from satellite optical data. Moreover, the use of the uncalibrated approach to obtain M pixels locations is a first step toward the application of the methodology on ungauged rivers. In order to achieve a fully uncalibrated procedure, the approach needs further testing on multiple study areas worldwide, to assess the obtained relationship and verify its applicability to different river regimes and areas. In addition, the role of vegetation should be properly addressed, also to avoid vegetated pixels being wrongly selected for M, as in the Montemolino station analysis (Figure 10c). Finally, a procedure to obtain the relationship between river discharge and CM-based proxies without observed data has yet to be developed. However, the good correlation between the obtained uncalibrated proxies and the observed river discharge indicates that their information could be already exploited as qualitative signals, thus allowing the assessment of temporal variability of river discharge (e.g., high flow and low flow periods) also on ungauged river systems.

Over gauged basins, estimated timeseries of river discharge can be obtained from CM indices using the space-based rating curve concept. Indeed, the CM-based proxies are different from the satellite measurements of hydraulic variables that exploit the same concept, such as altimeter river level data and satellite measurements of river width. CM/CMW, in fact, do not estimate directly a physical quantity and therefore they cannot be used directly in most available empiric or physical models. Nevertheless, also satellite river level and river width data have inherent limitations. Altimeters are characterized by lower temporal resolution and reduced spatial coverage with respect to optical sensors (Fekete et al., 2007; Tarpanelli et al., 2021). On the other hand, optical data cannot be used to obtain information on the river system in the presence of clouds. This issue is critical for river width estimation, which often lead the researchers to discard many satellite images by imposing strict thresholds on the presence of clouds (Feng et al., 2019), to consider cloud-free composite optical product with lower quality and temporal resolution (Elmi et al., 2015; 2021) or to obtain river width measurements from sensors that are not affected by clouds, such as microwave SAR (Synthetic Aperture Radar) sensors (Mengen et al., 2020). CM approaches, on the other hand, show less sensitivity to presence of clouds, due to the use of a masking procedure of the pixels affected by clouds and the averaging of large areas to obtain the values of the desired pixel values (e.g., in this study, images with 70 % of cloudy pixels were processed, whereas in Feng et al. 2019 all images with cloud percentage above 25 % were discarded). In addition, the techniques for estimating river width from satellite are usually based on a water/non-water binary characterization (Elmi et al., 2015; 2021; Feng et al., 2019; Mueller et al., 2016; Pavelsky et al., 2014; Sichangi et al., 2016), which limits the accuracy of the obtained river width measurement to the pixel size of the relative satellite. Instead, CM approaches exploit the measured reflectance values and should therefore theoretically allow for greater accuracy in river discharge estimates with respect to river width analysis. Each of the existing methodologies for estimating river discharge from satellite sensors has its own strengths and limitations, as river discharge is a rather complex variable to observe because of its relationship with multiple physical quantities. Synergies between the methodologies should be exploited to compensate their mutual weakness and maximize the accuracy of the obtained product (Sichangi et al, 2016; Tarpanelli et al., 2017). Future research should be oriented in this direction, to improve our ability to estimate river discharge from space.

5. Conclusions

Taking advantage of the high-resolution of Sentinel-2 data and their availability on Google Earth Engine platform, a modification of the CM approach to estimate river discharge from NIR satellite data was proposed. The method was enriched with the additional concept of exploiting a water (W) area to take in account the variation of sediment load in the river. The averaging of multiple pixels to obtain M timeseries was also proposed, to increase the methodology sensitivity to river discharge by avoiding as much as possible the condition of completely flooded or dry M. Four different configurations were applied for the selection of M pixels to test this concept, using as input Sentinel-2 data: three calibrated (1 pixel, 3x3 pixels and 9x9 pixels) against the observed river discharge, and one uncalibrated, based on selecting as M pixels those with low Spearman correlation with W or C. In order to test the advantages deriving from the use of Sentinel-2 high-resolution data, the single pixel calibration and the uncalibrated one were also tested by using as input the data from MODIS.

As a first step, a sensitivity analysis of each configuration thresholds was conducted at the station of Pontelagoscuro, over the Po River: the thresholds related to the extraction of the C- and W-masks had little incidence on the performance of the estimated river discharge and were fixed at the 5th percentile, while the ones related to the selection of M generated greater variability, proving that further research is needed to adapt the methodology to the different river regimes. The CM and CMW approaches were then applied over seven stations from two rivers in Italy: at Pontelagoscuro, Sermide, Borgoforte, Cremona and Piacenza along the Po River, and at Montemolino and Pontefelice along the Tiber River, for the period 2015-2020, exploiting the capacities of Google Earth Engine cloud platform. Results indicated a stable performance improvement of the CMW approach with respect to the CM approach for all the areas and configurations when Sentinel-2 data were adopted, proving the relevance of taking in account the sediments to correctly estimate the river discharge. The same advantages were not observed using MODIS data, due to the impossibility of correctly account for the sediment contribution when the satellite pixel size is similar or greater than the river width. Configuration 4 had proved the most effective at the Po River stations with respect to the calibrated ones. Over the Tiber River, instead, the uncalibrated procedure failed to detect the pixels sensitive to the variation of river discharge due to the presence of heavily vegetated pixels and the misregistration issues of the Sentinel-2 images: the apparent movement of the full area led to the selection of pixels that were not related to river discharge variation. The issue was present also at the Po River stations, but to a lesser degree and with a less severe impact due to the greater river width. Two additional sources of error were identified: the presence of cloud shadows and residual clouds not masked by the cloud masking procedure, and the variability of the value of C, due to, e.g., the effect of soil moisture variations or bidirectional reflectance effects.

This work represents a new step toward a non-calibrated methodology capable to obtain a river discharge proxy over ungauged river, thanks to the development of an uncalibrated methodology to derive the reflectance indices. The sediment contribution proved to be necessary to improve the river discharge estimation. Still, well registered and frequent NIR high-resolution data are fundamental to increase the accuracy of the retrievals. Further research is also needed to develop a relationship between the obtained uncalibrated proxy and the river discharge that does not need calibration, based, e.g., on model data or regionalization, in order to obtain a full uncalibrated methodology to estimate river discharge from space. Moreover, the need of testing the procedure over different study areas and understanding the role of the vegetation on river discharge estimation over highly vegetated cross sections should be also addressed, as well as the development of the procedure to obtain a better threshold selection and greater sensitivity to very high flows.

Acknowledgment

We would like to acknowledge Meteorological Environmental Earth Observation (MEEO) company for their role in download and subset Sentinel-2 images over Pontelagoscuro area. Also, we would like to acknowledge the support of European Space Agency (ESA) through the project STREAMRIDE (Contract no. CCN1 to 4000126745/19/I-NB)

References

Abdalla, S., Abdeh Kolahchi, A., Adusumilli, S., Aich Bhowmick, S., Alou-Font, E., Amarouche, L., … (2021) Altimetry for the future: Building on 25 years of progress, Advances in Space Research. Doi: https://doi.org/10.1016/j.asr.2021.01.022

Ahmed, R., Prowse, T., Dibike, Y., Bonsal, B., O'Neil, H. (2020). Recent Trends in Freshwater Influx to the Arctic Ocean from Four Major Arctic-Draining Rivers. Water 12, 1189. Doi: https://doi.org/10.3390/w12041189

Ahn J. H. and Park, Y. J. (2020). Estimating Water Reflectance at Near-Infrared Wavelengths for Turbid Water Atmospheric Correction: A Preliminary Study for GOCI-II. Remote Sensing 12(22), 3791. Doi: https://doi.org/10.3390/rs12223791

Belloni, R., Camici, S., Tarpanelli, A. (2021). Towards the continuous monitoring of the extreme events through satellite radar altimetry observations. Journal of Hydrology. In press. Doi: https://doi.org/10.1016/j.jhydrol.2021.126870

Bjerklie D. M., Lawrence Dingman S., Vorosmarty C. J., Bolster C. H., Congalton R. G. (2003). Evaluating the potential for measuring river discharge from space. Journal of Hydrology 278, 17–38. Doi: https://doi.org/10.1016/S0022-1694(03)00129-X

Bjerklie D. M., Moller D., Smith L. C., Dingman S. L. (2005). Estimating discharge in rivers using remotely sensed hydraulic information. Journal of Hydrology 309, 191–209. Doi: https://doi.org/10.1016/j.jhydrol.2004.11.022

Boergens, E., Buhl, S., Dettmering, D., Klüppelberg, C., Seitz, F. (2017). Combination of multi-mission altimetry data along the Mekong River with spatio-temporal kriging. Journal of Geodesy 91(5), 519-534. Doi: https://doi.org/10.1007/s00190-016-0980-z

Brakenridge, G. R., Nghiem, S. V., Anderson, E., Mic, R (2007). Orbital microwave measurement of river discharge and ice status. Water Resources Research 43, W04405. Doi: 10.1029/2006WR005238

Chandanpurkar H. A., Reager J. T., Famiglietti J. S., Syed T. H. (2017). Satellite- and Reanalysis-Based Mass Balance Estimates of Global Continental Discharge (1993–2015). Journal of Climate 30(21), 8481–8495. Doi: https://doi.org/10.1175/JCLI-D-16-0708.1

Crochemore, L., Isberg, K., Pimentel, R., Pineda, L., Hasan, A., Arheimer, B. (2020). Lessons learnt from checking the quality of openly accessible river flow data worldwide. Hydrological Sciences Journal 65(5), 699-711. Doi: https://doi.org/10.1080/02626667.2019.1659509

De Frasson R. P. M., Pavelsky T. M., Fonstad M. A., Durand M. T., Allen G. H., Schumann G., Lion C., Beighley R. E., Yang X. (2019) Global Relationships Between River Width, Slope, Catchment Area, Meander Wavelength, Sinuosity, and Discharge. Geophysical Research Letters 46(6), 3252–3262. Doi: https://doi.org/10.1029/2019GL082027

Domeneghetti, A., Tarpanelli, A., Grimaldi, L., Brath, A., Schumann, G. (2018). Flow Duration Curve from Satellite: Potential of a Lifetime SWOT Mission. Remote Sensing 10(7), 1107. Doi: https://doi.org/10.3390/rs10071107

Durand M., Neal J., Rodríguez E., Andreadis K. M., Smith L. C., Yoon Y. (2014). Estimating reach-averaged discharge for the River Severn from measurements of river water surface elevation and slope. Journal of Hydrology 511, 92–104. Doi: https://doi.org/10.1016/j.jhydrol.2013.12.050

Dziubanski D. J, Franz K. J. (2016). Assimilation of AMSR-E snow water equivalent data in a spatially-lumped snow model. Journal of Hydrology 540, 26–39. Doi: https://doi.org/10.1016/j.jhydrol.2016.05.046

Elmi O., Tourian M. J., Sneeuw N. (2015). River discharge estimation using channel width from satellite imagery. IEEE International Geoscience and Remote Sensing Symposium (IGARSS), 727-730. Doi: https://doi.org/10.1109/IGARSS.2015.7325867.

Elmi O., Tourian M. J., Bárdossy A., Sneeuw N. (2021). Spaceborne River Discharge From a Nonparametric Stochastic Quantile Mapping Function, Water Resources Research 57(12), e2021WR030277. Doi: https://doi.org/10.1029/2021WR030277

Emery C. M., Paris A., Biancamaria S., Boone A., Calmant S., Garambois P.-A., Santos da Silva J. (2018). Large-scale hydrological model river storage and discharge correction using a satellite altimetry-based discharge product. Hydrology and Earth System Sciences 22, 2135–2162. Doi: https://doi.org/10.5194/hess-22-2135-2018

Fekete, B. and Vörösmarty, C. (2007). The current status of global river discharge monitoring and potential new technologies complementing traditional discharge measurements. Proceedings of the Predictions in Ungauged Basins: PUB Kick-off (Proceedings of the PUB Kick-off meeting held in Brasilia, 20–22 November 2002). IAHS Publ. 309, 2007.

Fekete, B. M., Robarts, R. D., Kumagai, M., Nachtnebel, H. P., Odada, E., Zhulidov, A. V. (2015). Time for in-situ renaissance. Science 349, 685–686. Doi: https://doi.org/10.1126/science.aac7358.

Feng D., Gleason C. J., Yang X., Pavelsky T. M. (2019). Comparing discharge estimates made via the BAM algorithm in high-order Arctic rivers derived solely from optical CubeSat, Landsat, and Sentinel-2 data, Water Resources Research 55(9), 7753-7771. Doi: https://doi.org/10.1029/2019wr025599

Garambois P.-A., Monnier J. (2015). Inference of effective river properties from remotely sensed observations of water surface. Advances in Water Resources 79, 103–120. Doi: https://doi.org/10.1016/j.advwatres.2015.02.007

Gentile, F., Bisantino, T., Corbino, R., Milillo, F., Romano, G., Liuzzi, G. T. (2010). Monitoring and analysis of suspended sediment transport dynamics in the Carapelle torrent (southern Italy). Catena 80(1), 1–8. Doi: https://doi.org/10.1016/j.catena.2009.08.004

Gilvear, D., Hunter, P., Higgins, T. (2007). An experimental approach to the measurement of the effects of water depth and substrate on optical and near infra-red reflectance: A fieldbased assessment of the feasibility of mapping submerged instream habitat. International Journal of Remote Sensing. International Journal of Remote Sensing, 28(10), 2241-2256. Doi: https://doi.org/10.1080/01431160600976079.

Gleason C. J., Smith L. C. (2014). Toward global mapping of river discharge using satellite images and at-many-stations hydraulic geometry. Proceedings of the National Academy of Sciences 111(13), 4788–4791. Doi: https://doi.org/10.1073/pnas.1317606111

Gleason C. J., Garambois P. A., Durand M. (2017). Tracking River Flows from Space. Eos Transactions American Geophysical Union 99(1). Doi: https://doi.org/10.1029/2017EO078085

Gleason C. J., Durand M. T. (2020). Remote Sensing of River Discharge: A Review and a Framing for the Discipline. Remote Sensing, 12, 1107. Doi: https://doi.org/10.3390/rs12071107

Gorelick, N., Hancher, M., Dixon, M., Ilyushchenko, S., Thau, D., Moore, R. (2017). Google Earth Engine: Planetary-scale geospatial analysis for everyone. Remote sensing of Environment 202, 18-27. Doi: https://doi.org/10.1016/j.rse.2017.06.031

Hannah, D. M., Demuth, S., Van Lanen, H. A. J., Looser, U., Prudhomme, C., Rees, G., Stahl, K., Tallaksen, L. M. (2011). Large scale river flow archives: importance, current status and future needs. Hydrological Processes 25(7), 1191-1200. Doi: https://doi.org/10.1002/hyp.7794

Huo J., Qu X., Zhu D., Yuan Z., Zeng Z. (2021). Runoff monitoring in the Lhasa River Basin using passive microwave data, International Journal of Applied Earth Observation and Geoinformation 103, 102486. Doi: https://doi.org/10.1016/j.jag.2021.102486

Jodar J., Carpintero E., Martos-Rosillo S., Ruiz-Constan A., Marin-Lechado C., Cabrera-Arrabal J. A., Navarrete-Mazariegos E., Gonzalez-Ramon A., Lamban L. J., Herrera C., González-Dugo M. P. (2018). Combination of lumped hydrological and remote-sensing models to evaluate water resources in a semi-arid high altitude ungauged watershed of Sierra Nevada (Southern Spain). Science of Total Environment 625, 285–300. Doi: https://doi.org/10.1016/j.scitotenv.2017.12.300

Keesstra, S. D., Davis, J., Masselink, R. H., Casalí, J., Peeters, E. T., Dijksma, R. (2019). Coupling hysteresis analysis with sediment and hydrological connectivity in three agricultural catchments in Navarre, Spain. Journal of Soils and Sediments 19(3), 1598-1612. Doi: https://doi.org/10.1007/s11368-018-02223-0

Kremezi, M. and Karathanassi, V. (2019). Correcting the BRDF effects on Sentinel-2 ocean images. Proc. SPIE 11174, Seventh International Conference on Remote Sensing and Geoinformation of the Environment (RSCy2019), 111741C (27 June 2019). Doi: https://doi.org/10.1117/12.2533653

Larnier K., Monnier J., Garambois P.-A., Verley J. (2019). River Discharge and Bathymetry Estimations from SWOT Altimetry Measurements. Inverse Problems in Science and Engineering 29(6), 1-31. Doi: https://doi.org/10.1080/17415977.2020.1803858

Lin P., Pan M., Beck H. E., Yang Y., Yamazaki D., Frasson R., David C. H., Durand M., Pavelsky T. M., Allen G. H., Gleason C. J., Wood E. F. (2019). Global Reconstruction of Naturalized River Flows at 2.94 Million Reaches. Water Resources Research 55(8), 6499–6516. Doi: https://doi.org/10.1029/2019WR025287

Lopez P. L., Sutanudjaja E. H., Schellekens J., Sterk G., Bierkens M. F. P. (2017). Calibration of a large-scale hydrological model using satellite-based soil moisture and evapotranspiration products. Hydrology and Earth System Sciences 21, 3125–3144. Doi: https://doi.org/10.5194/hess-21-3125-2017

Malinowski, R., Groom, G., Schwanghart, W., Goswin, H. (2015). Detection and Delineation of Localized Flooding from WorldView-2 Multispectral Data. Remote Sensing 7, 14853-14875. Doi: https://doi.org/10.3390/rs71114853.

Mengen D., Ottinger M., Leinenkugel P., Ribbe L. (2020). Modeling River Discharge Using Automated River Width Measurements Derived from Sentinel-1 Time Series. Remote Sensing 12(19), 3236. Doi: https://doi.org/10.3390/rs12193236

Mueller N., Lewis A., Roberts D., Ring S., Melrose R., Sixsmith J., Lymburner L., McIntyre A., Tan P., Curnow S., Ip A. (2016). Water observations from space: Mapping surface water from 25 years of Landsat imagery across Australia, Remote Sensing of Environment 174, 341-352. Doi: https://doi.org/10.1016/j.rse.2015.11.003

Nash, J. E. and Sutcliffe, J. V. (1970). River Flow Forecasting through Conceptual Model. Part 1 - A Discussion of Principles. Journal of Hydrology, 10, 282-290. Doi: http://dx.doi.org/10.1016/0022-1694(70)90255-6

Neal J., Schumann G., Bates P., Buytaert W., Matgen P., Pappenberger F. (2009). A data assimilation approach to discharge estimation from space. Hydrological Processes 23(25), 3641–3649. Doi: https://doi.org/10.1002/hyp.7518

Nohara, D., Kitoh, A., Hosaka, M., Oki, T. (2006). Impact of Climate Change on River Discharge Projected by Multimodel Ensemble. Journal of Hydrometeorology 7(5), 1076-1089. Doi: https://doi.org/10.1175/JHM531.1

Oubanas H., Gejadze I., Malaterre P.-O., Mercier F. (2018). River discharge estimation from synthetic SWOT-type observations using variational data assimilation and the full Saint-Venant hydraulic model. Journal of Hydrology 559, 638–647. Doi: https://doi.org/10.1016/j.jhydrol.2018.02.004

Paris, A., Dias de Paiva, R., Santos da Silva, J., Medeiros Moreira, D., Calmant, S., Garambois, P. A., Collischonn, W., Bonnet, M. P., Seyler, F. (2016). Stage-discharge rating curves based on satellite altimetry and modeled discharge in the Amazon basin. Water Resources Research 52(5), 3787-3814. Doi: https://doi.org/10.1002/2014WR016618

Parr D., Wang G., Bjerklie D. (2015). Integrating Remote Sensing Data on Evapotranspiration and Leaf Area Index with Hydrological Modeling: Impacts on Model Performance and Future Predictions. Journal of Hydrometeorology 16(5), 2086–2100. Doi: https://doi.org/10.1175/JHM-D-15-0009.1

Pavelsky T. M. (2014). Using width-based rating curves from spatially discontinuous satellite imagery to monitor river discharge, Hydrological Processes 28, 3035-3040. Doi: https://doi.org/10.1002/hyp.10157

Pekel, J. F., Cottam, A., Gorelick, N., Belward, A. S. (2016). High-resolution mapping of global surface water and its long-term changes. Nature 540, 418–422. Doi: https://doi.org/10.1038/nature20584

Piecuch, C. G., Bittermann, K., Kemp, A. C., Ponte, R. M., Little, C. M., Engelhart, S. E., Lentz, S. J. (2018). River-discharge effects on United States Atlantic and Gulf coast sea-level changes. Proceedings of the National Academy of Sciences 115(30), 7729-7734. Doi: https://doi.org/10.1073/pnas.1805428115

Schwatke, C., Dettmering, D., Bosch, W., Seitz, F. (2015). DAHITI–an innovative approach for estimating water level time series over inland waters using multi-mission satellite altimetry. Hydrology and Earth System Sciences 19(10), 4345-4364. Doi: https://doi.org/10.5194/hess-19-4345-2015

Shi, Z., Chen, Y., Liu, Q., Huang, C. (2020). Discharge Estimation Using Harmonized Landsat and Sentinel-2 Product: Case Studies in the Murray Darling Basin. Remote Sensing 12(17), 2810. Doi: https://doi.org/10.3390/rs12172810

Sichangi A. W., Wang L., Yang K., Chen D., Wang Z., Li X., Zhou J., Liu W., Kuria D. (2016). Estimating continental river basin discharges using multiple remote sensing data sets, Remote Sensing of Environment 179, 36-53. Doi: https://doi.org/10.1016/j.rse.2016.03.019

Syed T. H., Famiglietti J. S., Chen J., Rodell M., Seneviratne S. I., Viterbo P., Wilson C. R. (2005). Total basin discharge for the Amazon and Mississippi River basins from GRACE and a land-atmosphere water balance. Geophysical Research Letters 32, L24404. Doi: https://doi.org/10.1029/2005GL024851

Tarpanelli, A., Brocca, L., Lacava, T., Melone, F., Moramarco, T., Faruolo, M., Pergola, N., Tramutoli, V. (2013). Toward the estimation of river discharge variations using MODIS data in ungauged basins. Remote Sensing of Environment 136, 47–55. Doi: https://doi.org/10.1016/j.rse.2013.04.010

Tarpanelli, A., Amarnath, G., Brocca, L., Massari, C., Moramarco, T. (2017). Discharge estimation and forecasting by MODIS and altimetry data in Niger-Benue River. Remote Sensing of Environment 195, 96–106. Doi: https://doi.org/10.1016/j.rse.2017.04.015

Tarpanelli, A., Iodice, F., Brocca, L., Restano, M., Benveniste, J. (2020). River Flow Monitoring by Sentinel-3 OLCI and MODIS: Comparison and Combination. Remote Sensing 12, 3867. Doi: https://doi.org/10.3390/rs12233867

Tarpanelli, A., Camici, S., Nielsen, K., Brocca, L., Moramarco, T., Benveniste, J. (2021). Potentials and limitations of Sentinel-3 for river discharge assessment. Advances in Space Research 68(2), 593-606. Doi: https://doi.org/10.1016/j.asr.2019.08.005

Tourian, M. J., Sneeuw, N., Bardossy, A. (2013). A quantile function approach to discharge estimation from satellite altimetry (ENVISAT). Water Resources Research 49(7), 4174–4186. Doi: https://doi.org/10.1002/wrcr.20348.

Tourian, M. J., Tarpanelli, A., Elmi, O., Qin, T., Brocca, L., Moramarco, T., Sneeuw, N. (2016). Spatiotemporal densification of river water level time series by multimission satellite altimetry. Water Resources Research 52, 1140-1159. Doi: https://doi.org/10.1002/2015WR017654.

Tourian, M. J., Schwatke, C., Sneeuw, N. (2017). River discharge estimation at daily resolution from satellite altimetry over an entire river basin. Journal of Hydrology 546, 230-247. Doi: https://doi.org/10.1016/j.jhydrol.2017.01.009.

Vörösmarty, C., Askew, A., Grabs, W., Barry, R. G., Birkett, C., Döll, P., Goodison, B., Hall, A., Jenne, R., Kitaev, L., Landwehr, J., Keeler, M., Leavesley, G., Schaake, J., Strzepek, K., Sundarvel, S. S., Takeuchi, K., Webster, F. (2001). Global water data: A newly endangered species. EOS Transactions 82, 54-54. Doi: https://doi.org/10.1029/01EO00031

Wagner, W., Lemoine, G., Rott, H. (1999). A method for estimating soil moisture from ERS scatterometer and soil data. Remote Sensing of Environment 70, 191–207. Doi: https://doi.org/10.1016/S0034-4257(99)00036-X

Wulf H., Bookhagen B., Scherler D. (2016). Differentiating between rain, snow, and glacier contributions to river discharge in the western Himalaya using remote-sensing data and distributed hydrological modeling. Advances in Water Resources 88, 152–169. Doi: https://doi.org/10.1016/j.advwatres.2015.12.004

Yang J., Huang X., Tang Q. (2020). Satellite-derived river width and its spatiotemporal patterns in China during 1990–2015, Remote Sensing of Environment 247, 111918. Doi: https://doi.org/10.1016/j.rse.2020.111918

Zakharova E., Nielsen K., Kamenev G., Kouraev A. (2020). River discharge estimation from radar altimetry: Assessment of satellite performance, river scales and methods, Journal of Hydrology 583, 124561. Doi: https://doi.org/10.1016/j.jhydrol.2020.124561

Zhang Y., Pan M., Wood E. F. (2016). On Creating Global Gridded Terrestrial Water Budget Estimates from Satellite Remote Sensing. Surveys in Geophysics 37, 249–268. Doi: https://doi.org/10.1007/s10712-015-9354-y